A computer model for sound propagation around conical seamounts

by

Jérémie Eskenazi

Submitted to the Department of Ocean Engineering
in partial fulfillment of the requirements for the degree of

Master of Science

at the

MASSACHUSETTS INSTITUTE OF TECHNOLOGY

January 2001

[February 2001]

Author .....
Department of Ocean Engineering
January 19, 2001

Certified by .....
Arthur B. Baggeroer
Ford Professor of Engineering,
Secretary of the Navy/Chief of Naval Operations
Chair for Ocean Sciences
Thesis Supervisor

Accepted by .....
Nicholas Patrikalakis
Kawasaki Professor of Engineering
Chairman, Departmental Committee on Graduate Students

A computer model for sound propagation around conical seamounts

by

Jérémie Eskenazi

Submitted to the Department of Ocean Engineering
on January 19, 2001, in partial fulfillment of the
requirements for the degree of
Master of Science

Abstract

This paper demonstrates a technique for computing the long-range sound pressure field around a penetrable conical seamount. The pressure field is generated by a harmonic point source. The seamount is positioned in a vertically stratified oceean. It is modeled as an outgrowth of the sediment layer covering the ocean bottom.

First, the seamount is decomposed into superposed rings of diameters increasing with the depth. Thus the problem reduces to a cylindrically layered system. Then, the method of normal modes is used to compute the sound pressure field in each layer.

In order to maintain numerical stability, the Direct Global Matrix approach is used. The radial eigenfunctions are expressed as functions of normalized Hankel and Bessel functions, and the linear system that arise is organized in an unconditionally stable matrix.

The results show a perturbation zone behind the seamount. It is bounded by two lines going from the source and tangent to the ring that is at the depth of the source. The values of the sound pressure inside the perturbation zone can be higher or lower than the values outside of it, according to the dimensions of the seamount.

This work was supported by the United States Navy, Office of Naval Research, under contract N00014-99-1-0087.

Thesis Supervisor: Arthur B. Baggeroer
Title: Ford Professor of Engineering,
Secretary of the Navy/Chief of Naval Operations
Chair for Ocean Sciences

Acknowledgments

This thesis is written in memory of my grandfather Haim Levy and my grandmother Sarah Eskenazi.

First, I thank my mother and father for supporting, guiding and above all, loving me. I especially thank my sister whose kindness and humour spice up my life.

Second, I thank my advisor Arthur B. Baggeroer for giving me this research topic and the ideas necessary to explore it.

Thanks to all the students and staff of MIT's Ocean Engineering Acoustics Group for their help. Thanks to Peter Daly for solving my first computer problems. Thanks to Yi-san Lai for his extraordinary patience when answering my questions. Thanks to David Ricks of Science Applications International Corporation for explaining to me the ideas in his thesis.

Also, I thank the friends who supported my exploration of the United States the most: Tom Scharfeld and Ian Ingram.

Finally, I thank all of my friends and family in France, Israel, and Spain, who give my life pleasure and meaning.

Contents

List of Figures

Chapter 1

Introduction

This thesis describes my research on the long-range underwater acoustic field around a conical seamount generated by a harmonic point source.

Long-range underwater acoustics is a particularly challenging field since usual acoustic equations require special mathematical and computational treatments to produce accurate results far from the source.

1.1 Motivation

My work was supported by the United States Navy, Office of Naval Research. Its general goal is the improvment of our understanding of underwater sound propagation.

A specific application of my research is the help on the detection of illegal underwater nuclear testing.

International organizations, like the Comprehensive Test Ban Treaty Organization (CTBTO), monitor global environments to ensure the respect of treaties banning experiments on nuclear weapons. Underwater nuclear tests release large amounts of acoustic energy (frequency 1-100 Hz) into the water. Because sound energy in the ocean is guided by temperature and density variations through the so-called SOFAR channel, the signals from underwater explosions can travel many thousands of kilometers and still have amplitudes large enough to be detected by underwater acoustic

sensors (hydrophones). The CTBT specifies a network of six hydrophones stations and five T-phase stations (island-based seismograph stations that can detect an ocean acoustic wave when it converts to a seismic wave upon striking the ocean bottom near the island). The hydroacoustic monitoring network has few sensors because of the high efficiency of the propagation of signals into the ocean.

My research is part of understanding how low-frequency sound waves travel around seamounts and thus determining if a seamount can screen the waves generated by an explosion.

1.2 Previous work

Acoustic perturbation by seamounts can be examined through experimentation and through theory. However, because of the complexity of the problem, both theories and experimental results that can be found in literature fail to provide clear views of the perturbation zones behind seamounts.

1.2.1 Experimental results

Nutile and Guthrie experimentally identified the acoustic shadowing by seamounts located north of the Hawaiian Ridge and explained it as the blockage of propagating rays by the seamounts [1].

More recently, Ebbeson and Turner measured the loss between a source and a multi-hydrophone receiving system over the Dickins Seamount in the Northeast Pacific Ocean [2]. Then Chapman and Ebbeson performed more measurements over the Dickins Seamount and concentrated on the study of the shadow zone that appear behind it [3]. Jensen *et al.* compared theoretical predictions, obtained with a Parabolic equation model, with the experimental transmission-loss data collected by Chapman and Ebbeson [4]. The agreement between theory and experiment was seen to be excellent.

All the measurements of the perturbation of the sound behind a seamount have two things in common:

- The data were always collected along a straight line going from the source and through the center of the seamount. Therefore, the results are insufficient to describe the shape of the perturbation zone behind the seamount.

- Experimental results always show that the perturbation zone is a shadow zone, i.e., a zone of lower sound pressure.

1.2.2 Theoretical approach of the problem

The effect of the seamount on long-range propagation can be qualitatively assessed from ray diagrams. Harrison derives analytical ray paths and shadow zone boundaries for some bottom topographies, including a seamount [5]. However, this method can not be a substitute for detailed analysis of intensity by normal mode theory.

Athanassoulis and Prospathopoulos present a normal mode solution for the three-dimensional problem of acoustic scattering from a nonpenetrable cylindrical island in shallow water [6]. Although their numerical simulations do not have the same dimensions as mine, their results about the number of azimuthal terms required to achieve numerical convergence as a function of the dimension of the environment will be useful to analyze the validity of my results (c.f. section 4.1.2).

The main inspiration for the modeling of the seamount and the normal mode solution exposed in this thesis comes from Taroukadis's work on the decomposition of the seamount into superposed rings [7]. Taroukadis's idea is to decompose the range-dependent environment into a cylindrically layered system of range-independent environments. However, this method can yield unstable equations and Taroukadis fails to get significant numerical results.

1.2.3 Direct Global Matrix approach

In order to obtain a stable system from Taroukadis's model, I use the Direct Global Matrix approach (DGM). DGM was developed for plane layered viscoelastic systems by Schmidt and Jensen [8], and applied to spherically layered systems by Schmidt [9] and to cylindrically layered system by Ricks and Schmidt [10].

DGM method allows the production of an unconditionally stable linear system by preventing the underflow and overflow of the solutions and by minimizing the propagation of errors.

1.3 Roadmap

Chapter Two, *The environment*, describes the ocean environment where the seamount is located.

Chapter Three, *Analytical formulation*, contains the analytical formulation of the problem.

Chapter Four, *Results*, describes and discusses the results.

Chapter Five, *Conclusion*, summarizes the results and offers suggestions for future work.

Appendix A contains the nomenclature followed in the mathematical developments.

Appendix B details the computing tools used to obtain the results.

Chapter 2

The environment

2.1 The waveguide

The seamount is located in an ocean modeled as a vertically stratified medium.

The ocean is an acoustic waveguide limited above by the sea surface and below by the sea floor. This waveguide can be modeled in many ways, according to what aspect of the sound propagation we want to focus on [4], [11]. I consider a three-layered waveguide as shown in Figure 2-1.

The waveguide is made of a surface, a bottom, a sediment layer, and a water column.

2.1.1 The sea surface

I consider the sea surface as a perfectly free boundary, with a Dirichlet boundary condition [12]. At the surface, the pressure becomes null:

$$p(surface) = 0. \tag{2.1}$$

Above the surface, I model the atmosphere as a vacuum. Because the difference between acoustic impedances in the water and in the air is large, there is no need for a more sophisticated model of the atmosphere in the top half-space.

My interest is in sound propagation at long range (on the order of hundreds of

Figure 2-1: The environment

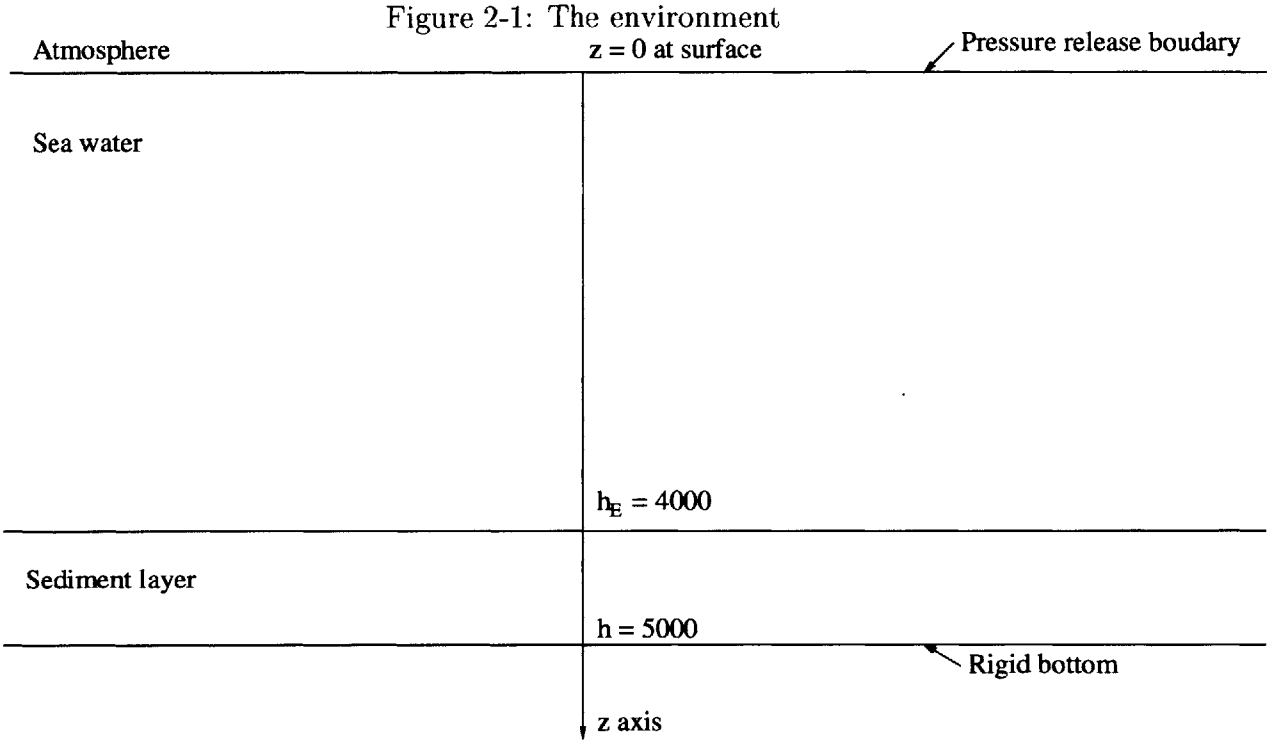

kilometers). Therefore I neglect surface scattering, which has significant effects only at short range.

2.1.2 The bottom

I assume that the bottom of the sediment layer is perfectly rigid. It verifies a Neumann boundary condition of the form

$$\frac{dp}{dz}(bottom) = 0, \tag{2.2}$$

which states that the normal component of the sediment particle velocity vanishes on the bottom.

2.1.3 The sediment layer

In the case of a three-dimensional propagation, an acoustic medium is characterized by its sound speed profile and its density.

I assume that the sediment layer is an isovelocity medium (i.e., the sound speed remains constant at any depth and range) with the following characteristics:

Table 2.1: The sediment layer environment

Top depth	4000 m
Bottom depth	5000 m
Sound speed	1600 m/s
Density	1100 kg/m^3

2.1.4 The seawater

In the seawater, I consider a constant density and a depth-dependent sound speed profile.

Table 2.2: The seawater environment

Top depth	0 m
Bottom depth	4000 m
Sound speed	$c(z)$
Density	1000 kg/m^3

Measurements have provided an empirical function for the sound speed profile c as a function of Temperature T, Salinity S, and depth z [13].

$$\begin{aligned} c =& 1448.96 + 4.951\,T - 5.304 \times 10^{-2}\,T^2 + 2.374 \times 10^{-4}\,T^3 \\ &+ 1.340\,(S-35) + 1.630 \times 10^{-2}\,z + 1.675 \times 10^{-7}\,z^2 \\ &- 1.025 \times 10^{-2}\,T\,(S-35) - 7.139 \times 10^{-13}\,T\,z^3 \end{aligned} \tag{2.3}$$

where T and S are functions of z.

I consider salinity to be constant: $S = 34.8$ parts/1000. I use a generic tempera-

ture profile in the open ocean [14]: $T(z)$ in °C is

$$T(z) = \begin{cases} \frac{-10}{1000}z + 15 \; for \; z \leq 1000m \\ \frac{4}{(h-1000)}(1000 - z) + 5 \; for \; z \geq 1000m \end{cases} \tag{2.4}$$

where h is the depth of the sediment layer ($h = 4000\,m$.) It produces a simple profile (Figure 2-2).

Figure 2-2: Temperature profile

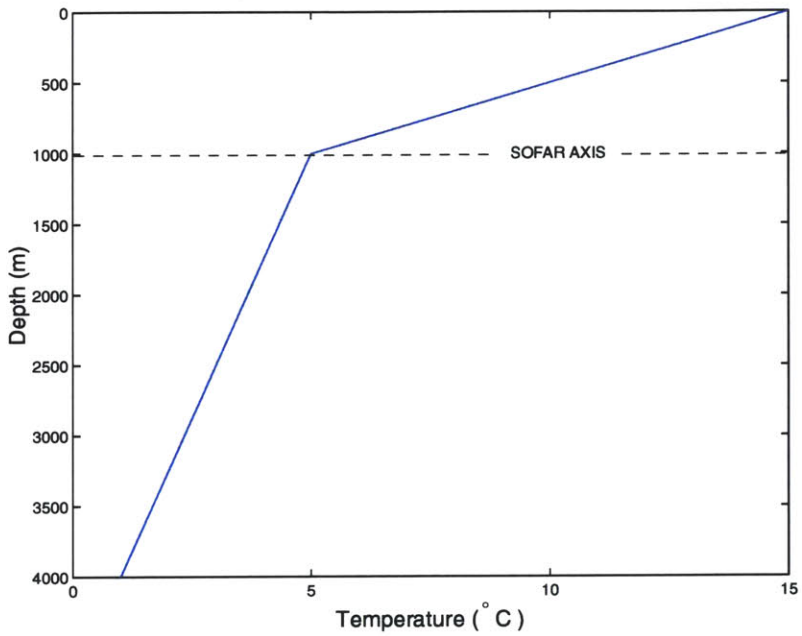

Again, I am interested in sound propagation at long range so I neglect temperature irregularities at the surface. The model does not take into account the temperature profile in the mixed layer (between 0 m and 100 m) where temperature varies greatly with the seasons.

The sound speed profile produced by such temperature and salinity profiles is shown in Figure 2-3. It forms a SOFAR duct at 1000 meters below the surface. The existence of a SOFAR duct allows long-range sound propagation since rays of sound launched above a certain angle will travel without bouncing on the waveguide boundaries and thus propagate with a lower transmission loss [15]. For this reason, I

Figure 2-3: Sound speed profile

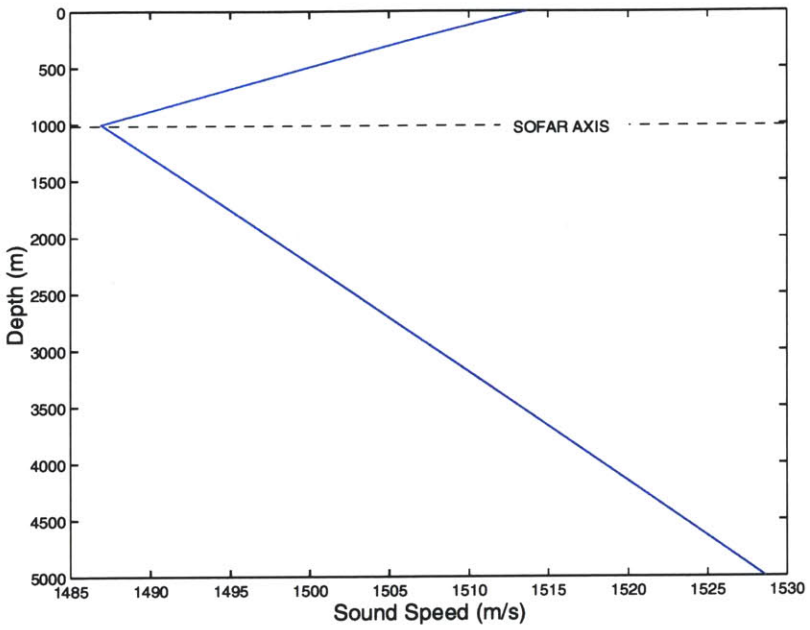

usually position my source at depth $z_0 = 1000\,m$.

2.2 The seamount

Taroukadis's model [7] is the benchmark for my research. Therefore, for the whole thesis, I will use the same notation as he does. The seamount in the ocean waveguide is under an acoustic wave generated by a point source, as depicted in Figure 2-4. It is modeled as an outgrowth of the sediment layer that covers the ocean bottom. I use the cylindrical-polar coordinates $\overrightarrow{r} = (r, \phi, z)$ with the z-axis oriented downward. The variables used to describe the environment follow:

Figure 2-4: The seamount

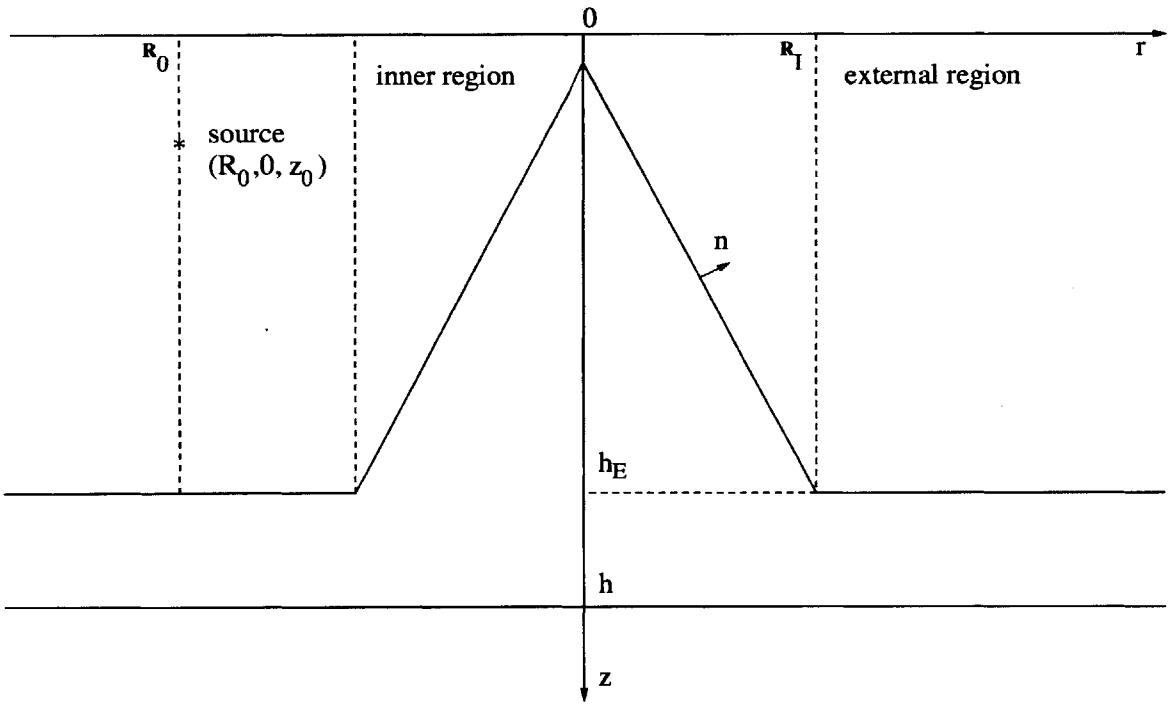

h	=	depth of the sea bottom
h_E	=	depth of the sediment layer
r_I	=	radius of the base of the seamount
ρ_1	=	density of water
ρ_2	=	density of the sediment layer
$\overrightarrow{n}$	=	unit normal vector outside the sediment layer
S_{bm}	=	surface of the seamount
S_b	=	surface of the sediment layer
$(R_0, 0, z_0)$	=	coordinates of the source
k	=	wavenumber $= \omega/c(z)$

The top of the seamount is 50 meters below the sea surface. The radius of the seamount R_I is equal to 10 kilometers.

For all numerical applications, I consider the source as a harmonic point source of frequency $f = 20Hz$.

The waveguide can be divided into two regions:

- an inner region for $r < R_I$, where the seamount is located,
- an external region for $r > R_I$.

We will see in chapter 3 how the waveguide can be further decomposed in order to solve the problem.

Chapter 3

Analytical formulation

Solving long-range sound propagation problems poses important mathematical challenges. Indeed, before any computation can be performed, it is important to find a way to handle the unstable equations that arise. Far from being restricted to my particular subject, the mathematical method described in this thesis can easily be applied to most acoustics problems involving multiple layers.

In the first part of this chapter, I will follow Taroukadis's work [7] for the analytical formulation of the pressure field. In the second part, I will provide details about the numerical treatment of loss mechanisms. In the third part, I will solve the equations obtained by Taroukadis using Schmidt and Jensen's normalization of the Hankel and Bessel functions [4]. Finally, in the fourth part, I will describe the linear system to solve and I will discuss the numerical stability of the method.

3.1 Taroukadis's approach to the problem

The benchmark for my research is the work of Taroukadis on sound propagation around conical seamounts [7]. Therefore, this subsection is just an application of Taroukadis's approach to the problem.

Assuming harmonic time-dependence for both the pressure field and the source,

the inhomogeneous wave equation governing the pressure field p is given by

$$\frac{\partial^2 p}{\partial r^2} + \frac{1}{r}\frac{\partial p}{\partial r} + \frac{1}{r^2}\frac{\partial^2 p}{\partial \phi^2} + \frac{\partial^2 p}{\partial z^2} - \frac{1}{\rho(z)}\frac{d\rho}{dz}\frac{\partial p}{\partial z} + \{k(r,z)\}^2 p = -\frac{1}{r}\delta(r - R_0)\delta(\phi)\delta(z - z_0). \tag{3.1}$$

There are many methods to solve Helmoltz equation. Among them, the normal modes theory is the most appropriate to solve problems in horizontally stratified media.

Using the method of normal modes, the solution of the wave equation is expressed in terms of radial and depth eigenfunctions:

$$p(r,z,\phi) = \sum_{n=1}^{\infty}\sum_{m=0}^{\infty} R_{mn}(r)U_n(z)\psi_m(\phi), \tag{3.2}$$

with ψ_m being a basis of sine functions, namely,

$$\psi_m(\phi) = e_m \sin(m\phi), \quad m = 0, 1, \ldots \tag{3.3}$$

where e_m is defined as follow

$$e_m = \begin{cases} \frac{1}{\sqrt{2\Pi}}, & m = 0 \\ \frac{1}{\sqrt{\Pi}}, & m \neq 0 \end{cases} \tag{3.4}$$

The circumferential eigenfunctions ψ_m are orthogonal:

$$\int_{-\pi}^{\pi} e_m \cos m\phi \;.\; e_n \sin n\phi \;\; d\phi = \delta_{mn}. \tag{3.5}$$

The depth eigenfunctions U_n satisfy the eigenvalue equation

$$\rho(z)\frac{d}{dz}\left[\frac{1}{\rho(z)}\right]\frac{dU_n(z)}{dz} + \left\{[k(z)]^2 - (k_n)^2\right\}U_n(z) = 0 \tag{3.6}$$

where k_n are discrete values of the horizontal wavenumber (or radial wavenumber)

associated with eigenfunctions U_n.

The depth eigenfunctions U_n can be scaled arbitrarily. I scale them so the norm C_n is unity, so the orthonormality of U_n with respect to the weighting function $\frac{1}{\rho(z)}$ yields

$$\int_0^h \frac{1}{\rho(z)} U_n(z).U_\nu(z)\, dz = \delta_{n\nu}. \tag{3.7}$$

Each mode has a non-vanishing field in the bottom. This is illustrated in figure 3-1 where the eigenfunction for the 38th mode is shown, as an example, in both the water column and the sediment layer for $r > R_I$. We will see in section 4.1.1, *Number of*

Figure 3-1: Eigenfunction for the 38th mode at $r > R_I$

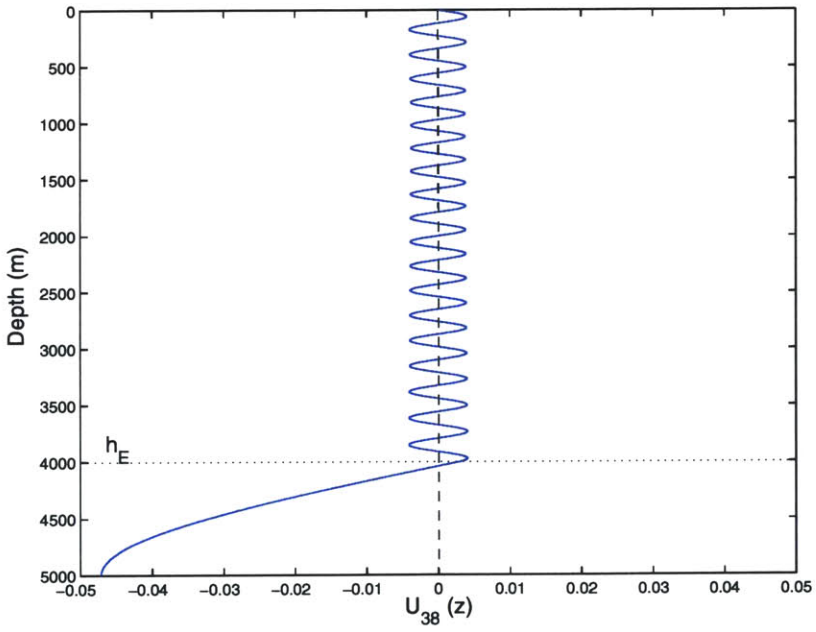

vertical modes, how this behavior allows us to lower the number of modes required for the convergence of the double series 3.2.

At this point, Taroukadis defines an inner region for $z \leq |R_I|$ and an external region for $z \geq |R_I|$ (c.f. Figure 2-4), in which he solves the homogeneous version of equation 3.1.

3.1.1 The inner region

The inner region, indicated by superscript I, contains no real source. Therefore, the wave equation to solve is the homogeneous Helmholtz equation, given by

$$\frac{\partial^2 p^I}{\partial r^2} + \frac{1}{r}\frac{\partial p^I}{\partial r} + \frac{1}{r^2}\frac{\partial^2 p^I}{\partial \phi^2} + \frac{\partial^2 p^I}{\partial z^2} - \frac{1}{\rho(z)}\frac{d\rho}{dz}\frac{\partial p^I}{\partial z} + \left\{k^I(r,z)\right\}^2 p^I = 0. \tag{3.8}$$

In this region, Taroukadis models the seamount as a superposition of I vertical rings of radii R_i. An example of the decomposition of the seamount into three rings is depicted in figures 3-2 and 3-3.

Figure 3-2: Decomposition of the seamount into three rings - side view

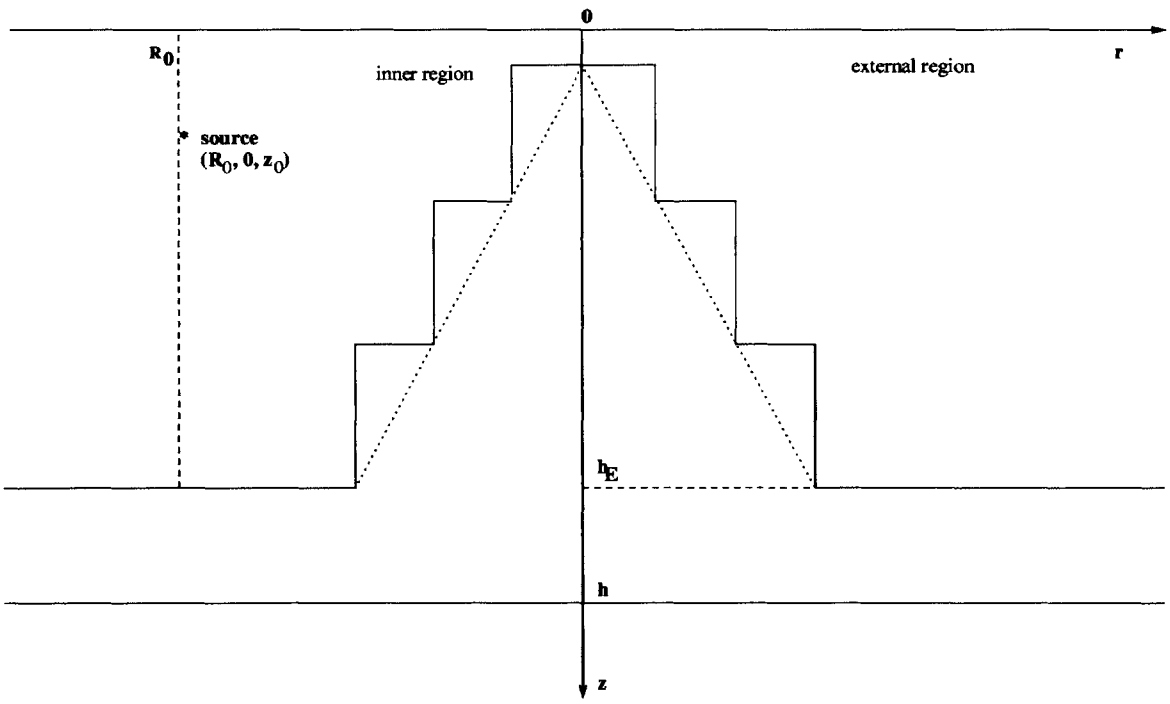

Obviously, the more the rings taken in the decomposition, the better the approximation.

For each ring i, it is thus possible to write the pressure field p_i^I as

$$p_i^I(r,z,\phi) = \sum_{n=1}^{\infty}\sum_{m=0}^{\infty} R_{mn}^{I,i}(r)U_{i,n}^I(z)\psi_m(\phi). \tag{3.9}$$

Figure 3-3: Decomposition of the seamount into three rings - top view

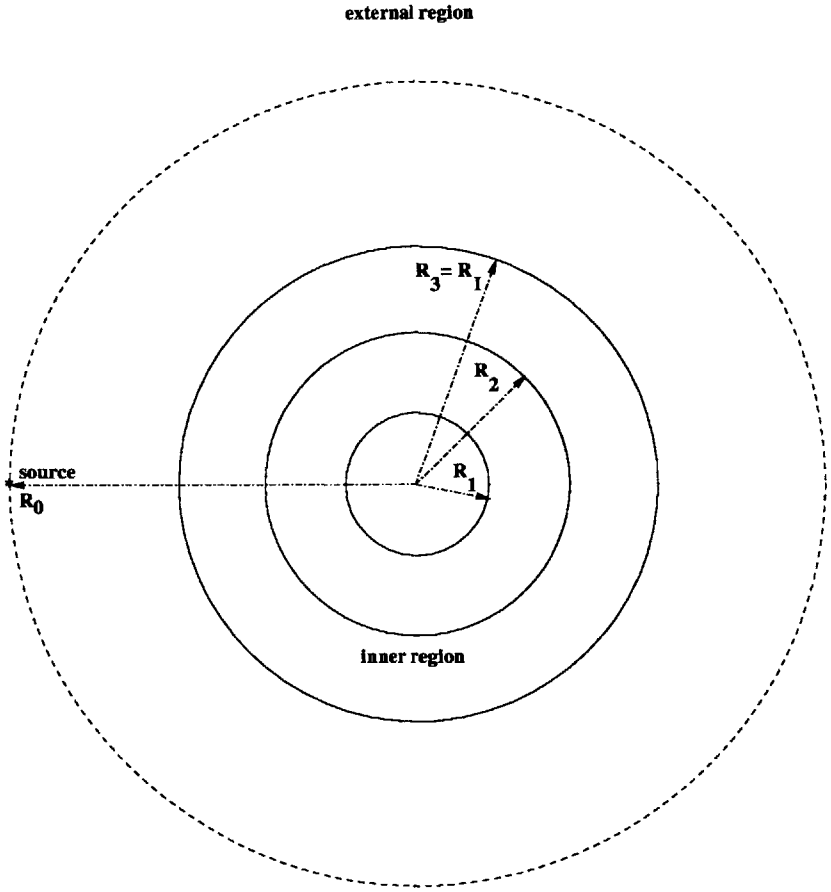

Substituting equation 3.9 in equation 3.8 gives

$$\sum_{n=1}^{\infty}\sum_{m=0}^{\infty} U_{i,n}^{I}(z)\psi_m(\phi)\left[\frac{d^2R_{mn}^{I,i}(r)}{dr^2}+\frac{1}{r}\frac{dR_{mn}^{I,i}(r)}{dr}-\frac{m^2}{r^2}R_{mn}^{I,i}(r)\right]$$
$$+R_{mn}^{I,i}(r)\psi_m(\phi)\left[\frac{d^2U_{i,n}^{I}(z)}{dz^2}-\frac{1}{\rho}\frac{d\rho}{dz}\frac{dU_{i,n}^{I}(z)}{dz}+(k^I)^2U_{i,n}^{I}(z)\right]=0. \qquad (3.10)$$

Inserting equation 3.6, multiplying by $\frac{1}{\rho(z)}U_{i,\nu}^{I}(z)$, integrating from 0 to h and using the orthonormality of the depth eigenfunctions 3.7, it is found that

$$\sum_{m=0}^{\infty}\psi_m(\phi)\left[\frac{d^2R_{m\nu}^{I,i}(r)}{dr^2}+\frac{1}{r}\frac{dR_{m\nu}^{I,i}(r)}{dr}+\left\{\left(k_{i,\nu}^{I}\right)^2-\frac{m^2}{r^2}\right\}R_{m\nu}^{I,i}(r)\right]=0. \qquad (3.11)$$

Multiplying by $\psi_\mu(\phi)$, integrating from $-\pi$ to π and using the orthogonality of the

circumferential eigenfunctions 3.5, it follows that

$$\frac{d^2}{dr^2}R^{I,i}_{\mu\nu}(r) + \frac{1}{r}\frac{d}{dr}R^{I,i}_{\mu\nu}(r) + \left[\left(k^I_{i,\nu}\right)^2 - \frac{\mu^2}{\nu^2}\right] R^{I,i}_{\mu\nu}(r) = 0 \tag{3.12}$$

for $r_{i-1} \leq r \leq R_i$ and $i = 1, 2, \ldots I$, where $k^I_{i,\nu}$ are the discrete values of the horizontal wavenumber associated with the eigenfunctions $U^I_{i,\nu}(z)$ of the ith ring.

Equation 3.12 is a Bessel equation of order μ for the function $R^{I,i}_{\mu\nu}(r)$ [16].

Taroukadis solves this equation with Hankel functions:

$$R^{I,i}_{\mu\nu}(r) = E^i_{\mu\nu}H^{(1)}_\mu\left(k^I_{i,\nu}r\right) + F^i_{\mu\nu}H^{(2)}_\mu\left(k^I_{i,\nu}r\right). \tag{3.13}$$

where $E^i_{\mu\nu}$ and $F^i_{\mu\nu}$ are some coefficients to be determined with the boundary conditions.

This solution is numerically unstable because of the behavior of Hankel functions for short ranges and high circumferential orders: if μ is greater than $k_\nu r$, then $H^{(1)}_\mu(k_\nu r)$ and $H^{(2)}_\mu(k_\nu r)$ approach infinity very quickly. Therefore, this method requires special numerical efforts to maintain numerical stability for large values of μ.

In section 3.3, I will demonstrate how numerical instability can be avoided using Schmidt's and Jensen's normalization of the Hankel functions.

3.1.2 The external region

In the external region, indicated by superscript E, the source must be taken into account. Therefore the equation to solve is the inhomogeneous wave equation 3.1.

Equation 3.2 can be re-written as

$$p^E(r, z, \phi) = \sum_{n=1}^{\infty}\sum_{m=0}^{\infty} R^E_{mn}(r)U^E_n(z)\psi^E_m(\phi). \tag{3.14}$$

The general method used in the calculus of equations 3.10, 3.11 and 3.12 still holds true, but the effects of the source must now be considered.

Substituting equation 3.14 in equation 3.1 gives

$$\sum_{n=1}^{\infty}\sum_{m=0}^{\infty} U_n^E(z)\psi_m(\phi)\left[\frac{d^2R_{mn}^E(r)}{dr^2}+\frac{1}{r}\frac{dR_{mn}^E(r)}{dr}-\frac{m^2}{r^2}R_{mn}^E(r)\right] + R_{mn}^E(r)\psi_m(\phi)\left[\frac{d^2U_n^E(z)}{dz^2}-\frac{1}{\rho}\frac{d\rho}{dz}\frac{dU_n^E(z)}{dz}+(k^I)^2U_n^E(z)\right] = -\frac{1}{r}\delta(r-R_0)\delta(\phi)\delta(z-z_0). \tag{3.15}$$

Plugging equation 3.6, multiplying by $\frac{1}{\rho(z)}U_\nu^E(z)$, integrating from 0 to h and using the orthonormality of the depth eigenfunctions 3.7 yields

$$\sum_{m=0}^{\infty}\psi_m(\phi)\left[\frac{d^2R_{m\nu}^E(r)}{dr^2}+\frac{1}{r}\frac{dR_{m\nu}^E(r)}{dr}+\left\{\left(k_\nu^E\right)^2-\frac{m^2}{r^2}\right\}R_{m\nu}^E(r)\right]=-\frac{1}{r}\delta(r-R_0)\delta(\phi)U_\nu^E(z_0). \tag{3.16}$$

Multiplying by $\psi_\mu(\phi)$, integrating from $-\pi$ to π and taking into account the orthogonality of the circumferential eigenfunctions 3.5, it follows that

$$\frac{d^2}{dr^2}\left[\frac{R_{\mu\nu}^E(r)}{\psi_\mu(0)\,U_\nu^E(z_0)}\right]+\frac{1}{r}\frac{d}{dr}\left[\frac{R_{\mu\nu}^E(r)}{\psi_\mu(0)\,U_\nu^E(z_0)}\right]+\left[\left(k_\nu^E\right)^2-\frac{\mu^2}{\nu^2}\right]\left[\frac{R_{\mu\nu}^E(r)}{\psi_\mu(0)\,U_\nu^E(z_0)}\right]=-\frac{1}{r}\delta(r-R_0) \tag{3.17}$$

where k_ν^E are the discrete values of the horizontal wavenumber associated with the eigenfunctions $U_\nu^E(z)$ of the external field .

Again, equation 3.17 is a Bessel equation of order μ for the function $\frac{R_{\mu\nu}^E(r)}{\psi_\mu(0)\,U_\nu^E(z_0)}$.

As for the internal field, Taroukadis solves Bessel equation with Hankel functions of the first and second kind:

$$\frac{R_{\mu\nu}^E(r)}{\psi_\mu(0)\,U_\nu^E(z_0)}=B_{\mu\nu}H_\mu^{(1)}\left(k_\nu^E r\right)+C_{\mu\nu}H_\mu^{(2)}\left(k_\nu^E r\right) \tag{3.18}$$

for $R_I \le r < R_0$, and

$$\frac{R_{\mu\nu}^E(r)}{\psi_\mu(0)\,U_\nu^E(z_0)}=D_{\mu\nu}H_\mu^{(1)}\left(k_\nu^E r\right) \tag{3.19}$$

for $r > R_0$.

As I indicate in section 3.1.1, these solutions are unstable for large values of μ. I use different solutions in section 3.3.

3.2 Numerical treatment of loss mechanisms

Complex wavenumber

We must take volumetric absortion into account in the computation of the sound pressure field. This is easily achived by manifesting the loss with a complex sound speed: $c(z) = c_0(z) + ic_1(z)$, where c_0 corresponds to the unperturbed sound speed profile. The wavenumber then becomes $k^2(z) = k_0^2(z) + ik_1^2(z) = \frac{\omega^2}{c^2(z)}$, that is,

$$k^2 = \underbrace{\frac{\omega^2}{c_0^2 + c_1^2}}_{k_0^2} + \underbrace{2i\omega^2 \frac{c_0 c_1}{[c_0^2 + c_1^2]^2}}_{ik_1^2}. \tag{3.20}$$

Computation of the imaginary part of the sound speed

Equations for material absorption in the water column are summarized by Urick [19]. If we assume that $c_1^2 \ll c_0^2$, then $c_1 \simeq \frac{\alpha}{\omega} c_0^2$ where α is the absorption coefficient in nepers/m.

A simplified expression of the absorption coefficient in the seawater as a function of the frequency f in kHz is

$$\alpha = \frac{1}{1000 \times 8.68589} \left(3.3 \times 10^{-3} + \frac{0.11 f^2}{1 + f^2} + \frac{44 f^2}{4100 + f^2} + 3 \times 10^{-4} f^2 \right) \quad \text{[nepers/m]}. \tag{3.21}$$

Thus in the water, $\alpha = 3.8550 \times 10^{-7}$ nepers/m for $f = .02$ kHz. The equivalent in dB/λ is $\alpha = 2.5113 \times 10^{-4}$ dB/λ.

In the sediment layer, the absorption coefficient as a function of f in kHz is

$$\alpha = \frac{1}{1000 \times 8.68589} 0.1 f \quad \text{[nepers/m]}. \tag{3.22}$$

Thus in the sediment layer, $\alpha = 2.3026 \times 10^{-4}$ nepers/m for $f = 20$ Hz. The equivalent in dB/λ is $\alpha = 0.1500$ dB/λ.

Computation of the imaginary part of the radial wavenumber

The introduction of a complex part to the wavenumber naturally affects the radial wavenumber, which becomes $k_n^2 = k_{n0}^2 + ik_{n1}^2$.

For the details of the computation of the imaginary part of the radial wavenumber k_{n1}, refer to Jensen *et al.* [4]. It is found that

$$ik_{n1}^2 = \int_0^h \frac{k_1^2(z)\, U_n^2(z)}{\rho(z)}\, dz. \tag{3.23}$$

Thus the radial wavenumber, which appears as an argument of the Hankel functions, is a complex number. Therefore, the solutions of Bessel equations 3.12 and 3.17 will decrease as the range r increases. This behavior represents the natural attenuation of sound as a function of range.

3.3 Normalization of Hankel functions

Problems of unstability that arise for large circumferential orders can be avoided by using the direct global matrix approach (DGM). DGM was developed for plane layered viscoelastic systems by Schmidt and Jensen [8], and applied to spherically layered systems by Schmidt [9] and to cylindrically layered systems by Ricks and Schmidt [10].

In our problem, since the seamount is decomposed into rings, the model reduces to a cylindrically layered system. (Cylindrical layers are visible in the top view of the seamount 3-3.) Therefore, DGM is well suited for the problem.

The first idea in DGM is the normalization of Hankel and Bessel functions. Bessel equation in the inner region (3.12) and in the external region (3.17) must be solved using particular sets of functions.

3.3.1 Solution in the inner region

General solutions to Bessel equation

Theoretically, solutions to Bessel equation in the inner region (3.12) can be any linear combination of two of the functions $J_\mu(x)$, $Y_\mu(x)$, $H_\mu^{(1)}(x)$, and $H_\mu^{(2)}(x)$ [17]. However, as explained by Ricks [18], only one pair can be chosen to avoid loss of distinction between asymptotic behaviors.

For $|x| \gg \mu$ (c.f. figure 3-4),

$$H_\mu^{(1)}(x) \sim \sqrt{2/(\pi x)}\, e^{i(x-\mu\pi/2-\pi/4)}$$
$$H_\mu^{(2)}(x) \sim 2J_\mu(x) \sim -2Y_\mu(x) \sim \sqrt{2/(\pi x)}\, e^{-i(x-\mu\pi/2-\pi/4)}$$

The loss of distinction between the functions J_μ, Y_μ and $H_\mu^{(2)}$ is illustrated in figure 3-4, where the functions of order $\mu = 1$ are drawn along the axis $\{x = a + ib\}_{a=b}$.

Figure 3-4: Hankel and Bessel functions for $\mu = 1$

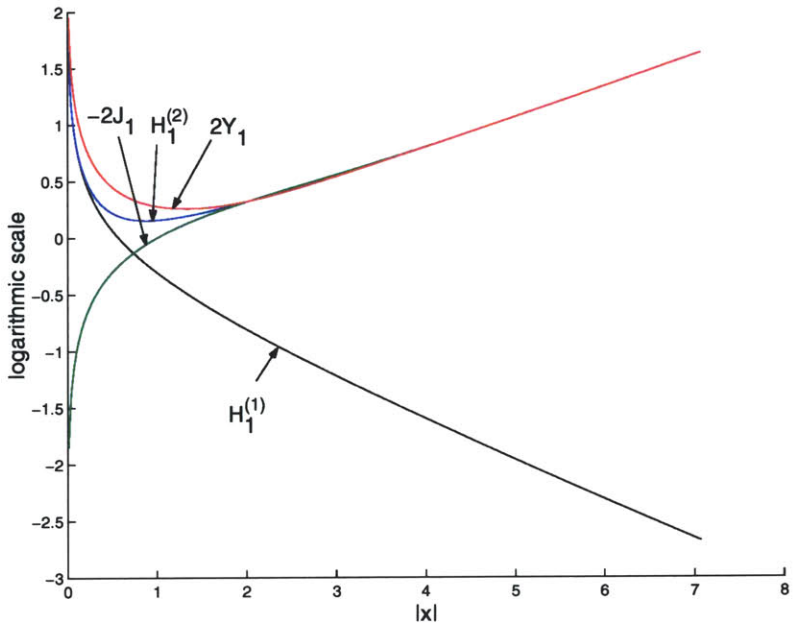

And for $|\mu| \gg |x|$,

$$J_\mu(x) \sim (x/2)^\mu / \Gamma(\mu+1)$$
$$Y_\mu(x) \sim -iH_\mu^{(1)}(x) \sim iH_\mu^{(2)}(x) \sim -(1/\pi)\,\Gamma(\mu)(x/2)^{-\mu}$$

Therefore, the only pair of function that preserves linear independence for both $|x| \gg \mu$ and $|\mu| \gg |x|$ is $H_\mu^{(1)}(x)$ and $J_\mu(x)$.

Normalization

I solve Bessel equation 3.12 with the following set of functions:

$$R_{\mu\nu}^{I,i}(r) = E_{\mu\nu}^i \frac{H_\mu^{(1)}\left(k_{i,\nu}^I r\right)}{H_\mu^{(1)}\left(k_{i,\nu}^I R_{i-1}\right)} + F_{\mu\nu}^i J_\mu\left(k_{i,\nu}^I r\right) H_\mu^{(1)}\left(k_{i,\nu}^I R_i\right) \quad \text{for } r \in [0; R_I]\,. \quad (3.24)$$

In the first ring $i = 1$, the sound pressure must be finite for $r = 0$. So the solution keeps only the Bessel function J_μ:

$$R_{\mu\nu}^{I,1}(r) = A_{\mu\nu} J_\mu\left(k_{1,\nu}^I r\right) H_\mu^{(1)}\left(k_{1,\nu}^I R_1\right) \quad \text{for } r \in [0; R_1]\,. \quad (3.25)$$

Note that solution 3.25 is part of the set of solutions 3.24 if we consider $E_{\mu\nu}^1 = 0$ and $F_{\mu\nu}^1 = A_{\mu\nu}$.

These normalized solutions provide numerical stability by doing two things:

1. For $\mu \gg |k_{i,\nu}^I r|$, they cancel the overflow of $H_\mu^{(1)}$ and the underflow of J_μ.
2. For $|k_{i,\nu}^I r| \gg \mu$, they reduce the influence of one boundary on an other when there is evanescence across layers.

I explain these two points in more details below.

To illustrate the first point, let us examine a numerical example. We will see in section 4.1.2, *Number of circumferential modes*, that μ can take values as high as 2600. For this numerical example, I take parameters that produce numbers that clearly represent the benefit of normalization: $\mu = 1000$, and $I = 20$. Without

normalization, we would have

$$H_{1000}^{(1)}\left(k_{10,1}^{I}R_{10}\right) = -3.3610 \times 10^{+257} + i \times -8.0828 \times 10^{+259},$$
$$\text{and} \quad J_{1000}\left(k_{10,1}^{I}R_{10}\right) = 4.3431 \times 10^{-264} + i \times 1.8064 \times 10^{-266}.$$

The overflow of the Hankel function and the underflow of the Bessel function lead to unstability in the system since computers can not multiply or divide such numbers without a significant loss of precision. The same numerical coefficients with normalization are

$$\frac{H_{1000}^{(1)}\left(k_{10,1}^{I}R_{10}\right)}{H_{1000}^{(1)}\left(k_{10,1}^{I}R_{9}\right)} = 1.1926 \times 10^{-42} + i \times 1.0102 \times 10^{-46},$$
$$\text{and} \quad J_{1000}\left(k_{10,1}^{I}R_{10}\right) H_{1000}^{(1)}\left(k_{10,1}^{I}R_{10}\right) = 3.4828 \times 10^{-10} + i \times -3.5105 \times 10^{-4}.$$

Thus, the number obtained are far enough from the computational limits of the computers.

To better understand the second point, let us consider as an example the case where $|k_{i,\nu}^{I}r| \gg \mu$. If there is evanescence across boudaries i.e., if $|\operatorname{Im}(k_{i,\nu}^{I}r)| \gg 1$, then close to the boundary $r = R_i$ between cylinder i and $(i+1)$,

$$\frac{H_{\mu}^{(1)}\left(k_{i,\nu}^{I}r\right)}{H_{\mu}^{(1)}\left(k_{i,\nu}^{I}R_{i-1}\right)} \ll J_{\mu}\left(k_{i,\nu}^{I}r\right) H_{\mu}^{(1)}\left(k_{i,\nu}^{I}R_{i}\right). \tag{3.26}$$

This means that the effect of boundary $r = R_i$ does not propagate far from it.

The same can be observed at boundary $r = R_{i-1}$. If $|k_{i,\nu}^{I}r| \gg \mu$ and $\operatorname{Im}(k_{i,\nu}^{I}r) \gg 1$, then close to the boundary,

$$\frac{H_{\mu}^{(1)}\left(k_{i,\nu}^{I}r\right)}{H_{\mu}^{(1)}\left(k_{i,\nu}^{I}R_{i-1}\right)} \gg J_{\mu}\left(k_{i,\nu}^{I}r\right) H_{\mu}^{(1)}\left(k_{i,\nu}^{I}R_{i}\right). \tag{3.27}$$

Again, in case of evanescence across boundaries, the effect of boundary $r = R_{i-1}$ does not propagate.

These solutions respect the physical idea that the effect of a boundary should not be perceveid far from it. In case of evanescence i.e., if the imaginary part of the wavenumber is great compared to 1, this reduces the propagation of errors from one boundary to an other and therefore maintains numerical stability.

In section 3.5 and figure 3-5, we will see how the final mapping of the system can implement the decoupling described above.

3.3.2 Solution in the external region

Equation 3.17 is solved similarily to equation 3.12.

For $r \in [R_I; R_0]$,

$$R^E_{\mu\nu}(r) = \left[B_{\mu\nu} \frac{H^{(1)}_\mu \left(k^E_\nu r\right)}{H^{(1)}_\mu \left(k^E_\nu R_I\right)} + C_{\mu\nu} J_\mu \left(k^E_\nu r\right) H^{(1)}_\mu \left(k^E_\nu R_0\right) \right] \psi_\mu(0)\, U^E_\nu(z_0). \tag{3.28}$$

For $r > R_0$, the sound pressure must go as $H^{(1)}_\mu \left(k^E_\nu r\right)$ to satisfy the radiation condition at infinity [16]. Therefore, the solution for $r > R_0$ is

$$R^E_{\mu\nu}(r) = \left[D_{\mu\nu} \frac{H^{(1)}_\mu \left(k^E_\nu r\right)}{H^{(1)}_\mu \left(k^E_\nu R_0\right)} \right] \psi_\mu(0)\, U^E_\nu(z_0). \tag{3.29}$$

As explained in section 3.3.1, these solutions provides numerical stability since they reduce the effects of boundaries into each other. To illustrate this behavior, let us take $|k^E_\nu r| \gg \mu$ and $r \simeq R_I$. Then, in the evanescent case where $\mathrm{Im}(k^E_\nu r) \gg 1$,

$$\frac{H^{(1)}_\mu \left(k^E_\nu r\right)}{H^{(1)}_\mu \left(k^I_\nu R_I\right)} \ll J_\mu \left(k^E_\nu r\right) H^{(1)}_\mu \left(k^E_\nu R_0\right). \tag{3.30}$$

And for $r \simeq R_0$,

$$\frac{H^{(1)}_\mu \left(k^E_\nu r\right)}{H^{(1)}_\mu \left(k^I_\nu R_I\right)} \gg J_\mu \left(k^E_\nu r\right) H^{(1)}_\mu \left(k^E_\nu R_0\right). \tag{3.31}$$

Thus, as in the inner region, these solution maintains numerical stability by:

1. Canceling the overflow of $H^{(1)}_\mu$ and the underflow of J_μ when $\mu \gg |k^E_\nu r|$.

2. Reducing the propagation of errors in case of evanescence across boundaries.

3.4 The source and boundary conditions

By replacing solutions 3.24, 3.25, 3.28 and 3.29 into the expression of the pressure 3.2, we have:

$$p_1^I(r,z,\phi) = \sum_{n=1}^{\infty}\sum_{m=0}^{\infty} A_{mn} J_m\left(k_{1,n}^I r\right) H_m^{(1)}\left(k_{1,n}^I R_1\right) U_{1,n}^I(z)\,\psi_m(\phi) \tag{3.32}$$

for $r \in [0; R_1]$,

$$p_i^I(r,z,\phi) = \sum_{n=1}^{\infty}\sum_{m=0}^{\infty}\left[E_{mn}^i \frac{H_m^{(1)}\left(k_{i,n}^I r\right)}{H_m^{(1)}\left(k_{i,n}^I R_{i-1}\right)} + F_{mn}^i J_m\left(k_{i,n}^I r\right) H_m^{(1)}\left(k_{i,n}^I R_i\right)\right] U_{i,n}^I(z)\,\psi_m(\phi) \tag{3.33}$$

for $r \in [R_1; R_I]$,

$$p^E(r,z,\phi) = \sum_{n=1}^{\infty}\sum_{m=0}^{\infty}\left[B_{mn}\frac{H_m^{(1)}\left(k_n^E r\right)}{H_m^{(1)}\left(k_n^E R_I\right)} + C_{mn} J_m\left(k_n^E r\right) H_m^{(1)}\left(k_n^E R_0\right)\right] U_n^E(z_0)\,\psi_m(0)\,U_n^E(z)\,\psi_m(\phi) \tag{3.34}$$

for $r \in [R_I; R_0]$, and

$$p^E(r,z,\phi) = \sum_{n=1}^{\infty}\sum_{m=0}^{\infty} D_{mn}\frac{H_m^{(1)}\left(k_n^E r\right)}{H_m^{(1)}\left(k_n^E R_0\right)} U_n^E(z_0)\,\psi_m(0)\,U_n^E(z)\,\psi_m(\phi) \tag{3.35}$$

for $r > R_0$.

Note that equations 3.32, 3.33 and 3.34 can be summarized in a single equation. If we define $E_{mn}^1 = A_{mn}$, $F_{mn}^1 = 0$, $E_{mn}^{I+1} = B_{mn}\,U_n^E(z_0)\,\psi_m(0)$, $F_{mn}^{I+1} = C_{mn}\,U_n^E(z_0)\,\psi_m(0)$, $p_{I+1}^I = p^E$, and $R_{I+1} = R_0$, we obtain an expression of the pressure

similar to equation 3.33 that is true for all $r \in [0; R_0]$:

$$p_i(r,z,\phi) = \sum_{n=1}^{\infty}\sum_{m=0}^{\infty}\left[E^i_{mn}\frac{H^{(1)}_m\left(k_{i,n}r\right)}{H^{(1)}_m\left(k_{i,n}R_{i-1}\right)} + F^i_{mn}J_m\left(k_{i,n}r\right)H^{(1)}_m\left(k_{i,n}R_i\right)\right]U_{i,n}(z)\,\psi_m(\phi). \tag{3.36}$$

To solve the problem, we need to approximate the solutions by taking a finite number of vertical modes n and circumferential modes m in the expression of the pressure field. If we take N vertical modes and $M+1$ circumferential modes, then we have $2 \times N \times (I+1) \times (M+1)$ unknown coefficients A, E, F, C, and D. We need the same number of source and boundary conditions to be able to solve the problem.

3.4.1 The boundary conditions

Continuity of pressure

At boundary $r = R_i$, the continuity of pressure yields

$$p_i(R_i,z,\phi) = p_{i+1}(R_i,z,\phi) \quad \text{for } i = 1,2,\ldots,I. \tag{3.37}$$

This means that the acoustic pressure must be continuous between the rings.

We replace the pressure by its series expression 3.36 and we limit the calculus to the first N vertical modes and $M+1$ circumferential modes. Multiplying equation 3.37 by $e_\mu cos\phi$, integrating from $-\pi$ to π and using the orthogonality of the circumferential eigenfunctions, we obtain a set of $M+1$ equations,

$$\sum_{n=1}^{N}\left[E^i_{\mu n}\frac{H^{(1)}_\mu\left(k_{i,n}R_i\right)}{H^{(1)}_\mu\left(k_{i,n}R_{i-1}\right)} + F^i_{\mu n}J_\mu\left(k_{i,n}R_i\right)H^{(1)}_\mu\left(k_{i,n}R_i\right)\right]U_{i,n}(z) = \sum_{n=1}^{N}\left[E^{i+1}_{\mu n} + F^{i+1}_{\mu n}J_\mu\left(k_{i+1,n}R_i\right)H^{(1)}_\mu\left(k_{i+1,n}R_{i+1}\right)\right]U_{i,n}(z). \tag{3.38}$$

Multiplying equation 3.38 by $\frac{1}{\rho_i(z)}U_{i,\nu}$, integrating from 0 to h and exploiting the

orthonormality of the vertical eigenfunctions, we get a set of $N \times (M+1)$ equations

$$E^i_{\mu\nu} \frac{H^{(1)}_\mu (k_{i,\nu} R_i)}{H^{(1)}_\mu (k_{i,\nu} R_{i-1})} + F^i_{\mu\nu} J_\mu (k_{i,\nu} R_i) H^{(1)}_\mu (k_{i,\nu} R_i) =$$
$$\sum_{n=1}^{N} E^{i+1}_{\mu n} Z^{i,i+1}_{n,\nu} + \sum_{n=1}^{N} F^{i+1}_{\mu n} J_\mu (k_{i+1,n} R_i) H^{(1)}_\mu (k_{i+1,n} R_{i+1}) Z^{i,i+1}_{n,\nu}. \quad (3.39)$$

Continuity of the normal component of fluid particle velocity

The continuity of the normal component of fluid particle velocity at interface $r = R_i$ produces

$$\frac{1}{\rho_i} \frac{\partial p_i}{\partial r}(R_i, z, \phi) = \frac{1}{\rho_{i+1}} \frac{\partial p_{i+1}}{\partial r}(R_i, z, \phi) \quad \text{for } i = 1, 2, \ldots, I. \quad (3.40)$$

By doing the same operations as between equations 3.37 and 3.39, we obtain

$$E^i_{\mu\nu} k_{i,\nu} \frac{\frac{dH^{(1)}_\mu}{dr} (k_{i,\nu} R_i)}{H^{(1)}_\mu (k_{i,\nu} R_{i-1})} + F^i_{\mu\nu} k_{i,\nu} \frac{dJ_\mu}{dr} (k_{i,\nu} R_i) H^{(1)}_\mu (k_{i,\nu} R_i) =$$
$$\sum_{n=1}^{N} E^{i+1}_{\mu n} k_{i+1,\nu} \frac{\frac{dH^{(1)}_\mu}{dr} (k_{i+1,\nu} R_i)}{H^{(1)}_\mu (k_{i+1,\nu} R_{i-1})} \Delta Z^{i,i+1}_{n,\nu}$$
$$+ \sum_{n=1}^{N} F^{i+1}_{\mu n} k_{i+1,\nu} \frac{dJ_\mu}{dr} (k_{i+1,n} R_i) H^{(1)}_\mu (k_{i+1,n} R_{i+1}) \Delta Z^{i,i+1}_{n,\nu}. \quad (3.41)$$

For each interface, there are $N \times (M+1)$ equations 3.39 and $N \times (M+1)$ equations 3.41. The continuity conditions at the boundaries thus yield $2 \times N \times I \times (M+1)$ equations.

3.4.2 The source condition

If we multiply equation 3.17 by r, we obtain a Sturm-Liouville equation of the form

$$s \nabla^2 u + \nabla s \nabla u - q u = -\rho F \quad (3.42)$$

where $s(r) = r$ and $u(r) = \frac{R^E_{\mu\nu}(r)}{\psi_\mu(0)\, U^E_\nu(z_0)}$. Equation 3.42 implies two continuity conditions at $r = R_0$ [20]:

$$u(R_0^+) = u(R_0^-) \tag{3.43}$$

and

$$\frac{du}{dr}(R_0^+) - \frac{du}{dr}(R_0^-) = -\frac{1}{s(R_0)}. \tag{3.44}$$

Replacing $R^E_{\mu\nu}(r)$ by its expressions 3.28 and 3.29, equation 3.43 becomes

$$B_{\mu\nu}\frac{H^{(1)}_\mu(k_\nu R_0)}{H^{(1)}_\mu(k_\nu R_I)} + C_{\mu\nu} J_\mu(k_\nu R_0)\, H^{(1)}_\mu(k_\nu R_0) = D_{\mu\nu}, \tag{3.45}$$

and equation 3.44 becomes

$$B_{\mu\nu}\frac{\frac{dH^{(1)}_\mu}{dr}(k_\nu R_0)}{H^{(1)}_\mu(k_\nu R_I)} + C_{\mu\nu}\frac{dJ_\mu}{dr}(k_\nu R_0)\, H^{(1)}_\mu(k_\nu R_0) = D_{\mu\nu}\frac{\frac{dH^{(1)}_\mu}{dr}(k_\nu R_0)}{H^{(1)}_\mu(k_\nu R_0)} - \frac{1}{R_0}. \tag{3.46}$$

To compute the derivatives of J and H, we use the recurrent relation

$$\mathcal{C}'_\mu(z) = -\mathcal{C}_{\mu+1}(z) + \frac{\mu}{z}\mathcal{C}_\mu(z) \tag{3.47}$$

where $\mathcal{C}$ denotes J or H [17].

Solving the set of equations 3.45 and 3.46, we find that $C_{\mu\nu}$ can be separated and expressed as a function of the Wronskian of J_μ and H_μ:

$$C_{\mu\nu} = \frac{-1}{k_\nu R_0\, W\left[H_\mu(k_\nu R_0); J_\mu(k_\nu R_0)\right]}, \tag{3.48}$$

A trivial calculation gives $W\left[H_\mu(k_\nu R_0); J_\mu(k_\nu R_0)\right] = \frac{-2i}{\pi k_\nu R_0}$, and thus

$$C_{\mu\nu} = \frac{-i\pi}{2} \tag{3.49}$$

We can also compute $B_{\mu\nu}$ as a function of $D_{\mu\nu}$ and $C_{\mu\nu}$

$$B_{\mu\nu} = D_{\mu\nu}\frac{H_\mu^{(1)}(k_\nu R_I)}{H_\mu^{(1)}(k_\nu R_0)} - C_{\mu\nu}J_\mu(k_\nu R_0)\,H_\mu^{(1)}(k_\nu R_I) \tag{3.50}$$

Thus, at the interface $r = R_0$, we have a total of $2 \times N \times (M+1)$ equations 3.49 and 3.50. With equations 3.39 and 3.41, we have a total of $2 \times N \times (I+1) \times (M+1)$ source and boundary conditions, for the same number of unknown. Therefore, the linear problem can be solved.

As we can see in equation 3.50, $B_{\mu\nu}$ and $D_{\mu\nu}$ are directly related since we know the value of $C_{\mu\nu}$. So in order to decrease the dimension of the system, we can exclude the unknowns $D_{\mu\nu}$ and equations 3.50 of the system. The dimension of the system then reduces to $N \times (2I+1) \times (M+1)$.

3.5 The matrices

Equations 3.39, 3.41 and 3.49 form a linear system for the unknowns A, E, F, and C. Therefore, they can be put on the form

$$\mathcal{A}.X = \mathcal{B} \tag{3.51}$$

$\mathcal{A}$ is a matrix of dimension $[N \times (2I+1) \times (M+1)]^2$ and $\mathcal{B}$ are vectors of dimension $N \times (2I+1) \times (M+1)$. X is the vector of the unknowns and $\mathcal{B}$ is the vector of the forcing terms due to the presence of the source.

3.5.1 Decoupling of the system

We can see that the system is uncoupled among circumferential orders μ or m. Therefore, it can be split into $M+1$ sub-systems of dimension $N \times (2I+1)$. For each circumferential order $\mu = 0, 1, \ldots, M$, we need to solve a system of the form

$$\mathcal{A}_\mu.X_\mu = \mathcal{B}_\mu \tag{3.52}$$

$\mathcal{A}_\mu$ are matrices of dimension $[N \times (2I+1)]^2$. X_μ are the vectors of the unknowns $A_{\mu\nu}$, $E_{\mu\nu}$, $F_{\mu\nu}$, and $C_{\mu\nu}$, for $\nu = 1, 2, \ldots, N$ and μ fixed.

3.5.2 Mapping of the matrices

For a given μ, I take X_μ as follow:

$$X_\mu = \begin{bmatrix} \begin{bmatrix} A_{\mu,1} \\ \vdots \\ A_{\mu,N} \end{bmatrix} \\ \begin{bmatrix} E^i_{\mu,1} \\ \vdots \\ E^i_{\mu,N} \\ F^i_{\mu,1} \\ \vdots \\ F^i_{\mu,N} \end{bmatrix}_{i\in[2;N]} \\ \begin{bmatrix} B_{\mu,1} \\ \vdots \\ B_{\mu,N} \end{bmatrix} \\ \begin{bmatrix} C_{\mu,1} \\ \vdots \\ C_{\mu,N} \end{bmatrix} \end{bmatrix} \tag{3.53}$$

Therefore matrix $\mathcal{A}_\mu$ is a combination of lines $\mathcal{L}^1_{\mu\nu}$, $\Delta\mathcal{L}^1_{\mu\nu}$, $\mathcal{L}^i_{\mu\nu}$, $\Delta\mathcal{L}^i_{\mu\nu}$, and $\mathcal{L}^{I+1}_{\mu\nu}$.

$$\mathcal{A}_\mu = \begin{bmatrix} \begin{bmatrix} \mathcal{L}^1_{\mu,1} \\ \Delta\mathcal{L}^1_{\mu,1} \\ \vdots \\ \mathcal{L}^1_{\mu,N} \\ \Delta\mathcal{L}^1_{\mu,N} \end{bmatrix} \\ \begin{bmatrix} \mathcal{L}^i_{\mu,1} \\ \Delta\mathcal{L}^i_{\mu,1} \\ \vdots \\ \mathcal{L}^i_{\mu,N} \\ \Delta\mathcal{L}^i_{\mu,N} \end{bmatrix}_{i\in[2;N]} \\ \begin{bmatrix} \mathcal{L}^{I+1}_{\mu,1} \\ \vdots \\ \mathcal{L}^{I+1}_{\mu,N} \end{bmatrix} \end{bmatrix} \tag{3.54}$$

The lines are described below.

$$\mathcal{L}^1_{\mu\nu} = [\underbrace{0\cdots0}_{\nu-1}\{J_\mu(k_{1\nu}R_1)H_\mu(k_{1\nu}R_1)\}\underbrace{0\cdots0}_{N-\nu}$$
$$\underbrace{\left(-Z^{1,2}_{n\nu}\right)_{n=1,\ldots,N}}_{N}\underbrace{\left(-J_\mu(k_{2\nu}R_1)H_\mu(k_{2\nu}R_2)Z^{1,2}_{n\nu}\right)_{n=1,\ldots,N}}_{N}\underbrace{0\cdots0}_{2N(I-1)}] \tag{3.55}$$

$$\Delta\mathcal{L}^1_{\mu\nu} = [\underbrace{0\cdots0}_{\nu-1}\left(\frac{dJ_\mu}{dr}(k_{1\nu}R_1)H_\mu(k_{1\nu}R_1)\right)\underbrace{0\cdots0}_{N-\nu}$$
$$\underbrace{\left(-k_{2,\nu}\frac{\frac{dH_\mu}{dr}(k_{2\nu}R_1)}{H_\mu(k_{2\nu}R_1)}\Delta Z^{1,2}_{n\nu}\right)_{n=1,\ldots,N}}_{N}\underbrace{\left(-J_\mu(k_{2\nu}R_1)H_\mu(k_{2\nu}R_2)Z^{1,2}_{n\nu}\right)_{n=1,\ldots,N}}_{N}\underbrace{0\cdots0}_{2N(I-1)}] \tag{3.56}$$

$$\mathcal{L}^i_{\mu\nu} = [\underbrace{0\cdots0}_{2Ni-3N+\nu-1}\left(\frac{H_\mu(k_{i\nu}R_i)}{H_\mu(k_{i\nu}R_{i-1})}\right)\underbrace{0\cdots0}_{N-1}(J_\mu(k_{i\nu}R_i)H_\mu(k_{i\nu}R_i))\underbrace{0\cdots0}_{N-\nu}$$
$$\underbrace{\left(-Z^{i,i+1}_{n\nu}\right)_{n=1,\ldots,N}}_{N}\underbrace{\left(-J_\mu(k_{i+1,\nu}R_i)H_\mu(k_{i+1,\nu}R_{i+1})Z^{i,i+1}_{n\nu}\right)_{n=1,\ldots,N}}_{N}\underbrace{0\cdots0}_{2N(I-1)}] \tag{3.57}$$

$$\Delta\mathcal{L}^i_{\mu\nu} = [\underbrace{0\cdots0}_{2Ni-3N+\nu-1}\left(k_{i\nu}\frac{\frac{dH_\mu}{dr}(k_{i\nu}R_i)}{H_\mu(k_{i\nu}R_{i-1})}\right)\underbrace{0\cdots0}_{N-1}\left(k_{i\nu}\frac{dJ_\mu}{dr}(k_{i\nu}R_i)H_\mu(k_{i\nu}R_i)\right)\underbrace{0\cdots0}_{N-\nu}$$
$$\underbrace{\left(-k_{i+1,\nu}\frac{\frac{dH_\mu}{dr}(k_{i+1,\nu}R_i)}{H_\mu(k_{i+1,\nu}R_i)}\Delta Z^{i,i+1}_{n\nu}\right)_{n=1,\ldots,N}}_{N}$$
$$\underbrace{\left(-k_{i+1,\nu}\frac{dJ_\mu}{dr}(k_{i+1,\nu}R_i)H_\mu(k_{i+1,\nu}R_{i+1})\Delta Z^{i,i+1}_{n\nu}\right)_{n=1,\ldots,N}}_{N}\underbrace{0\cdots0}_{2N(I-1)}] \tag{3.58}$$

$$\mathcal{L}^{I+1}_{\mu\nu} = [\underbrace{0\cdots0}_{2NI+\nu-1}\ 1\ \underbrace{0\cdots0}_{N-\nu}] \tag{3.59}$$

$\mathcal{B}_\mu$ is a simple vector containing zeros and values of $C_{\mu\nu}$ that we calculated in

equation 3.49:

$$\mathcal{B}_\mu = \begin{bmatrix} 0 \\ \vdots \\ \vdots \\ 0 \\ \frac{-i\pi}{2} \\ \vdots \\ \frac{-i\pi}{2} \end{bmatrix} \tag{3.60}$$

As an example of the form of the matrices obtained, Figure 3-5 shows matrix $\mathcal{A}_1$ for a decomposition of the seamount into 4 rings and $N = 110$. It displays the logarithm of the absolute value of the dimensionless terms of the matrix. Except for the first and last blocks in the diagonal, the matrix is diagonal with blocks of the form of **G**, **H**, **I** and **J** (c.f. Figure 3-5). **G** is made of the terms

$$\left(-Z_{n\nu}^{i,i+1}\right)_{n=1,\dots,N} \text{ and } \left(-k_{i+1,\nu}\frac{\frac{dH_\mu}{dr}(k_{i+1,\nu}R_i)}{H_\mu(k_{i+1,\nu}R_i)}\Delta Z_{n\nu}^{i,i+1}\right)_{n=1,\dots,N}$$

H is composed of

$$\left(-J_\mu(k_{i+1,\nu}R_i)H_\mu(k_{i+1,\nu}R_{i+1})Z_{n\nu}^{i,i+1}\right)_{n=1,\dots,N}$$
$$\text{and } \left(-k_{i+1,\nu}\frac{dJ_\mu}{dr}(k_{i+1,\nu}R_i)H_\mu(k_{i+1,\nu}R_{i+1})\Delta Z_{n\nu}^{i,i+1}\right)_{n=1,\dots,N}$$

I is a diagonal line of the terms

$$\left(\frac{H_\mu(k_{i\nu}R_i)}{H_\mu(k_{i\nu}R_{i-1})}\right) \text{ and } \left(k_{i\nu}\frac{\frac{dH_\mu}{dr}(k_{i\nu}R_i)}{H_\mu(k_{i\nu}R_{i-1})}\right)$$

and **J** is a diagonal line of the terms

$$\left(J_\mu(k_{i\nu}R_i)H_\mu(k_{i\nu}R_i)\right) \text{ and } \left(k_{i\nu}\frac{dJ_\mu}{dr}(k_{i\nu}R_i)H_\mu(k_{i\nu}R_i)\right)$$

Figure 3-5: Example of a matrix $\mathcal{A}_\mu$: Matrix $\mathcal{A}_1$ for a decomposition of the seamount into 4 rings

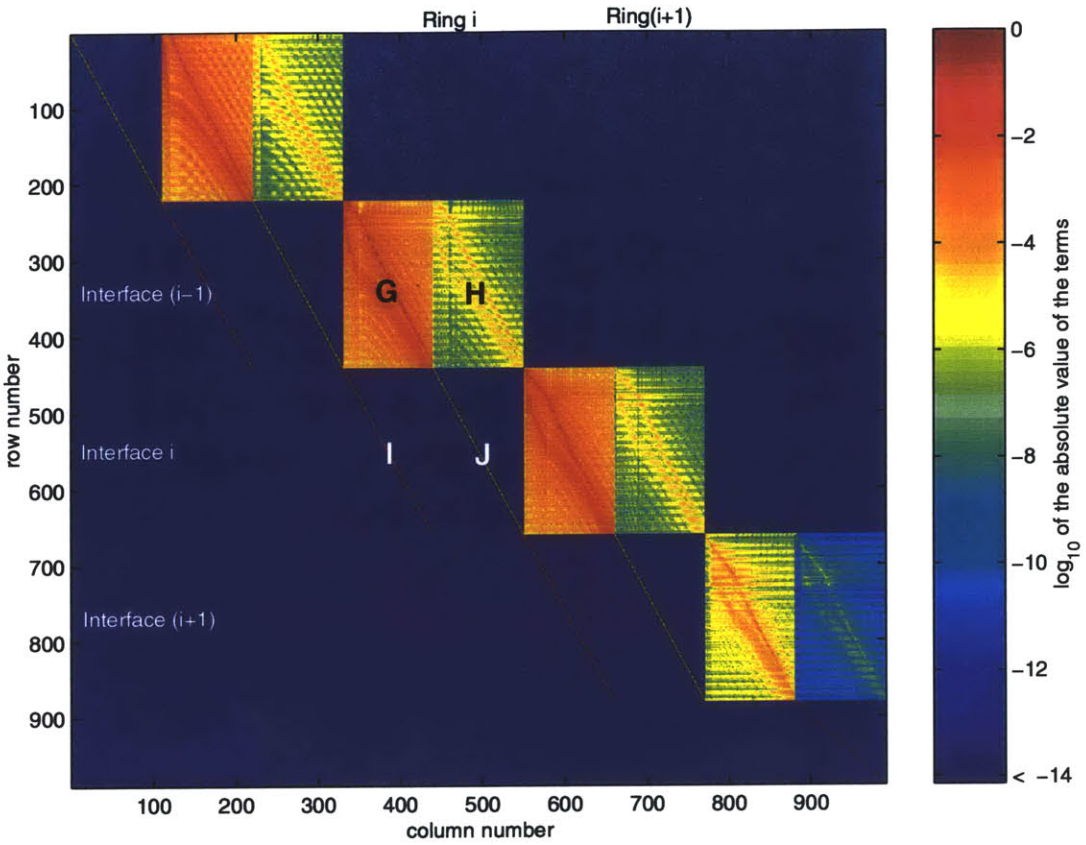

In this example, the imaginary part of the wavenumber is too small to consider that there is enough evanescence to reach the conditions of inequalities 3.26 and 3.27 in section 3.3.1. If there were a stronger evanescence, the values in block **I** would have been less than the values in block **J**. Thus, because the values in **G** are greater than the values in **H**, all the blocks of highest values would have been located along the diagonal of the matrix, making the solution more stable.

However, this is not the case here: The evanescent condition $\mathrm{Im}(k_{i\nu}) \gg 1$ is reached for greater wavenumbers (higher frequencies) or greater absorption coefficients. Thus, for the values that I use in the numerical applications, normalization of the Hankel and Bessel functions is mainly useful to avoid overflow of Hankel functions H and underflow of Bessel functions J.

Chapter 4

Results

I recall that, for all computations, I took $f = 20$ Hz.

4.1 Discussion of the number of modes

In order to compute the pressure, we must find the modes for which there is convergence of the double series 3.2.

4.1.1 Number of vertical modes

To compute the vertical eigenfunctions in the waveguide, I used the *Kraken Normal Mode Program* [21]. The maximum number of modes in the waveguide increases with the depths of the rings. The maximum number of modes in the region of the inner ring ($r < R_1$) is 125 and the maximum number of modes in the region outside the seamount ($r > R_0$) is 132. Therefore, the maximum number of modes that I can consider is 125.

Two different minimum mode numbers are required in the problems:

- The minimum number of modes needed to fill the matrices $\mathcal{A}_\mu$ and solve the linear systems $\mathcal{A}_\mu.X_\mu = \mathcal{B}_\mu$ (3.52),

- The minimum number of modes needed to compute the double series 3.2 with enough precision.

Number of vertical modes in the matrix

In order to compute the unknowns $E^i_{\nu\mu}$ and $F^i_{\nu\mu}$, we need to fill the matrices $\mathcal{A}_\mu$ and to solve the corresponding linear systems. The more vertical modes N we include in the computation, the more accurate the results. I noticed that the convergence of the vector of unknowns X_μ as a function of the number of modes is rather slow: It occurs only after the 110th mode. Therefore, I take 110 modes into account to fill the matrix and solve the linear systems 3.52.

Number of vertical modes in the double series

In order to reduce the dimension of the system (and therefore reduce the time of the computation), we need to determine the minimum number of vertical modes required to achieve computation of the double series 3.2 with enough accuracy. The double series 3.2 converges quickly when the vertical eigenfunctions hit the sediment layer; that is, when the attenuation becomes strong enough to cancel propagation. Thus, there exist a vertical mode N for which

$$p(r,z,\phi) \simeq \sum_{n=1}^{N}\sum_{m=0}^{\infty} R_{mn}(r)U_n(z)\psi_m(\phi). \tag{4.1}$$

This happens when the imaginary part of the wavenumber is great enough: if $|\operatorname{Im}(k^I_{i,\nu}r)| \gg 1$, the sound propagation attenuates very rapidly.

As an example, figure 4-1 shows $|\operatorname{Im}(k_{i,\nu})|$ as a function of modes for a decomposition of the seamount into 4 rings.

The greater the ring number, the deeper the sea bottom. Therefore, when the ring number i increases, the mode number N_i at which the loss becomes significant increases. Thus, the minimum mode to take into account is the mode for which there is strong attenuation in the region $r > R_I$, where the sea floor is the deepest. From figure 4-1, we see that $N = 35$. The depth of region $r > R_I$ does not change with the

Figure 4-1: Imaginary part of the radial wavenumber in function of modes, in m^{-1}

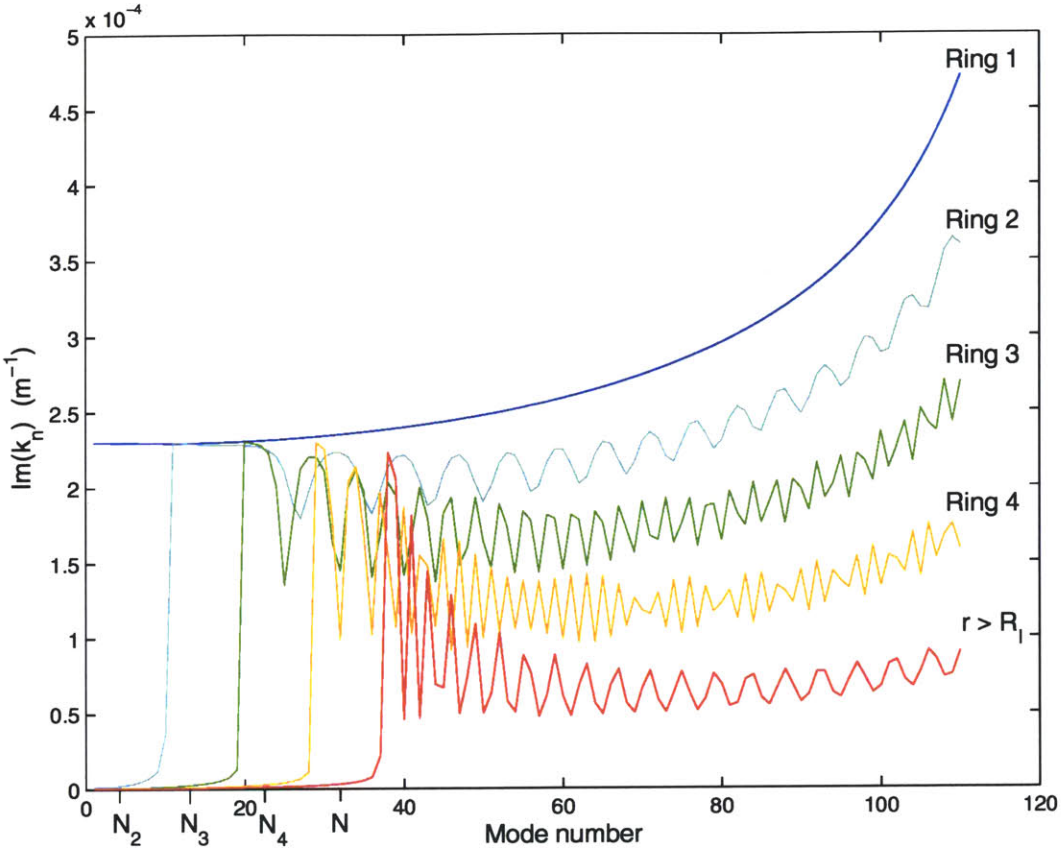

number of rings so the maximum number of vertical modes taken into account in the double series remains 35 for other computations with different numbers of rings.

4.1.2 Number of circumferential modes

To determine the maximum circumferential order M to take into account in the computation of the pressure, I compute the pressure for fixed circumferential orders:

$$p_\mu(r, z, \phi) = \sum_{n=1}^{N} R_{\mu n}(r) U_n(z) \psi_\mu(\phi). \tag{4.2}$$

Figure 4-2 is an example of the results obtained at the position of the source, for $I = 20$ rings and $N = 125$. In this example, p_μ becomes negligible after the

Figure 4-2: Pressure at the source as a function of circumferential order

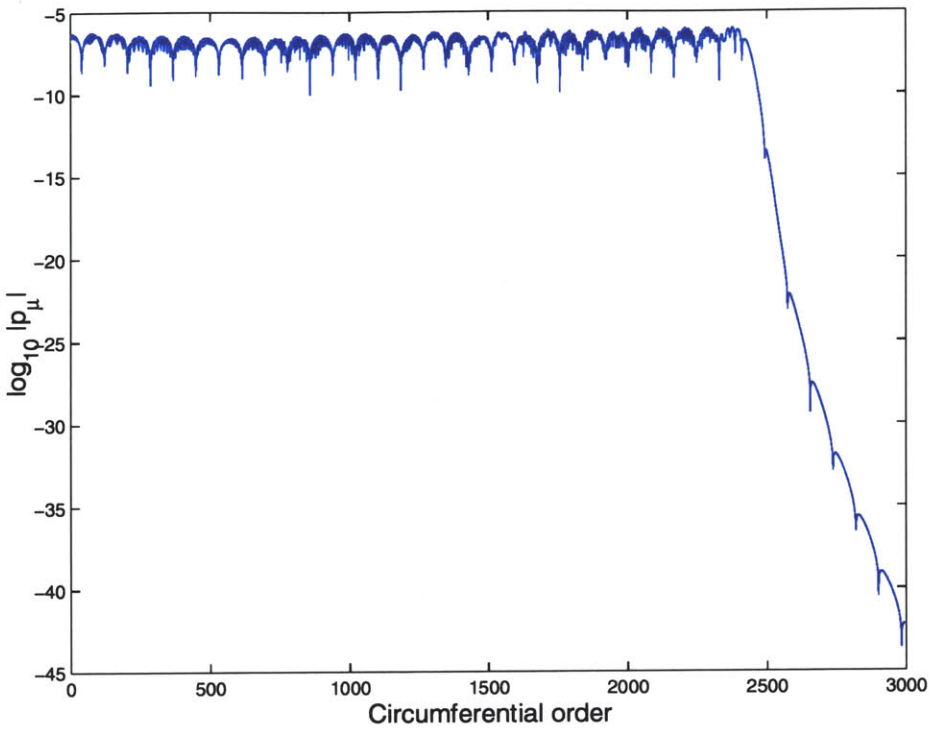

2600th circumferential order. There are similar results for all other points in the environment, so considering $M = 2600$ for computing the pressure at every range and depth produces precise results.

Athanassoulis and Prospathopoulos studied the minimum number of circumferential orders M required to achieve numerical convergence as a function of the dimension of the problem, in the case of a cylindrical island [6]. They found that M increases proportionally to kR_I. They studied some environments for which $kR_I \in [4; 84]$ and determined $M \in [20; 200]$.

Our problem is larger since $kR_I = 838$ for $R_I = 10\,\text{km}$, but I still find that the value of M increases with the dimensions of the problem. For example, we would need to take $M = 5400$ for a seamount of base radius $R_I = 15\,\text{km}$. However, I did not study seamounts with base radius greater than 10 km because they would have been physically unrealistic.

4.2 Special cases

In order to check the validity of both the theory and my computer code, it was necessary to apply them to particular well-known cases.

4.2.1 Back scattering

Figure 4-3: Back scattering

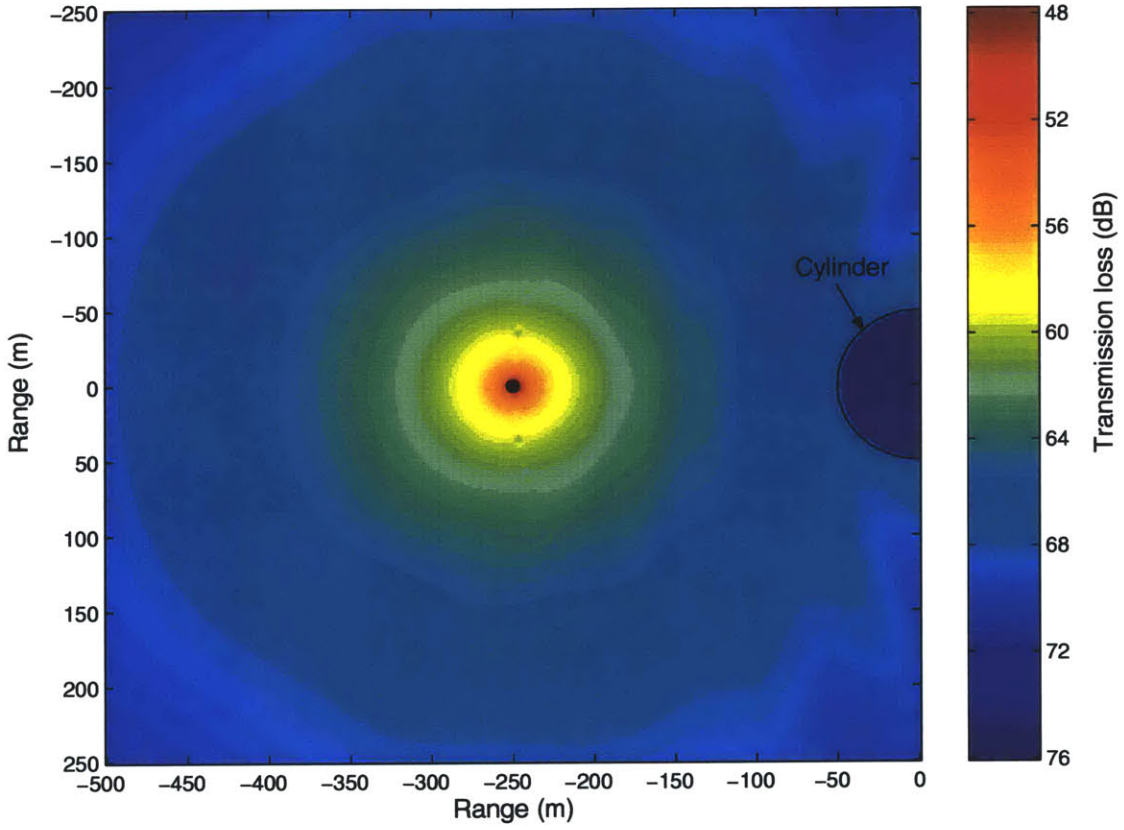

Parameters: I = 1. R_I = 50 m. Depth = 1000 m. Source at (-250 m, 0, 1000 m).

When the sound field hits the seamount, a pencil of sound is beamed backward and its anglewidth is proportional to $\frac{1}{R_I}$. Therefore, if we take R_I small enough, we can observe the back scattering of the sound. This is illustrated in figure 4-3, in a case where the seamount is reduced to a cylinder of diameter $R_I = 50\,\text{m}$. The source is positioned at $R_0 = -250\,\text{m}$ and the receivers are at the depth of the source (1000 m).

The results are expressed in terms of *transmission loss*, defined as

$$\mathrm{TL} = -20 \log_{10} \left| \frac{p}{p_{ref}} \right|, \tag{4.3}$$

where p_{ref} is a pressure reference: $p_{ref} = 1\,\mathrm{Pa}$.

The sound field looks perturbed between the source and the cylinder, which proves that the model is precise enough to compute the effects of back scattering. In later examples, I use a much greater R_I, so back scattering becomes too small to be observed.

4.2.2 No seamount in the waveguide

Figure 4-4: No seamount in the waveguide

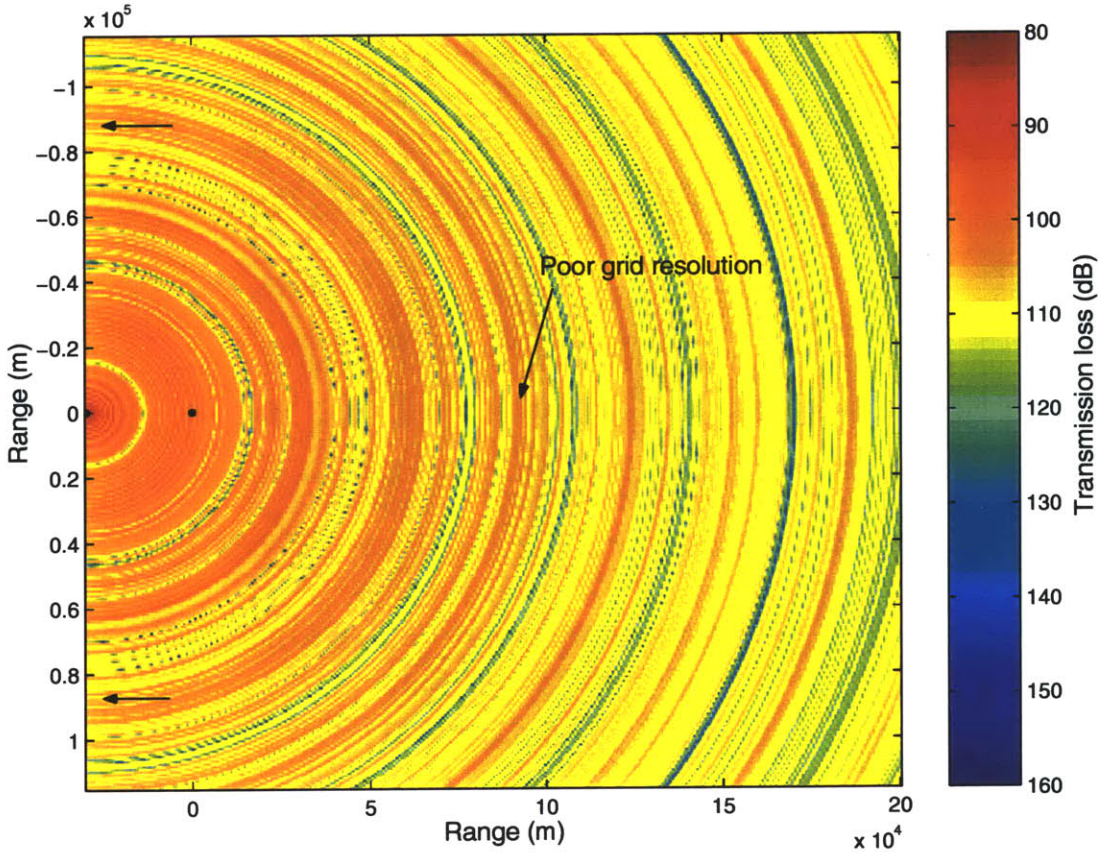

Parameters: I = 1. R_I = .5 m. Depth = 1000 m. Source at (-3000 m, 0, 1000 m).

Figure 4-4 shows the results obtained when the seamount is a small cylinder of radius 50 cm. A black dot indicates the position of the cylinder.

The cylinder is too small compared to the wavelength to have a noticeable effect on the computation of the sound propagation. Therefore, this case is equivalent to the case where there is no seamount in the waveguide.

In figure 4-4, we can notice some perturbation zones, indicated by arrows. They are only due to the precision of the grid: the more points in the grid, the less visible these "perturbations." Because the time of the numerical simulation increases with the precision of the grid, it has to be limited. I am using 600 points in the grid, which is the limit precision for which I can obtain results in a reasonable amount of time.

In cylindrical coordinates, the spreading loss between the source and a point (r, ϕ, z) is $H = 10 \times \log \frac{r}{r_{ref}}$ where $r_{ref} = 1\,\text{m}$. In the case of figure 4-4, the right-hand limit of the region under consideration is at $r = 200\,\text{km}$, so H should be in the order of 50 dB there. The results show the transmission loss varying from about 80 dB at the source to 125 dB at 200 km far from the source, which corresponds to $H \simeq 45\,\text{dB}$. Thus the cylindrical spreading loss is within the order of the theoretical predictions. Moreover, these results are close to those obtained for similar problems [4].

Filling of the environment as a function of circumferential orders

We can notice the way the sound is computed as a function of circumferential orders by comparing figures 4-5, 4-6, and 4-7. Figure 4-5 shows the results for μ varying from 0 to 100. Figure 4-6 shows the results for μ varying from 0 to 400. Figure 4-7 shows the results for μ varying from 0 to 1300. As μ increases, the computation produces results that fill the environment starting from axis $\phi = 0$ and cylindrically spreading toward axes $\phi = \frac{\pi}{2}$ and $\phi = \frac{-\pi}{2}$.

Figure 4-5: No seamount. $\mu = 0 \ldots 100$

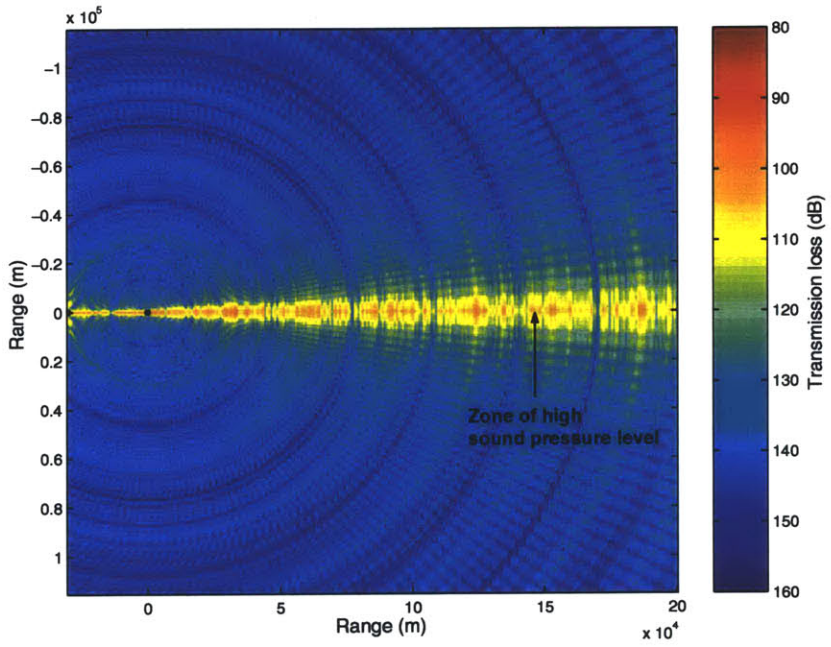

Parameters: I = 1. R_I = .5 m. Depth = 1000 m. Source at (-3000 m, 0, 1000 m).

We can see that the results inside the zones of high sound pressure level near axis $\phi = 0$ are identical to final results. In other words, the computation for circumferential orders greater than a given μ_1 have little effect on the results obtained in the zone of high sound pressure level for μ varying between 0 and μ_1.

Figure 4-6: No seamount. $\mu = 0 \ldots 400$

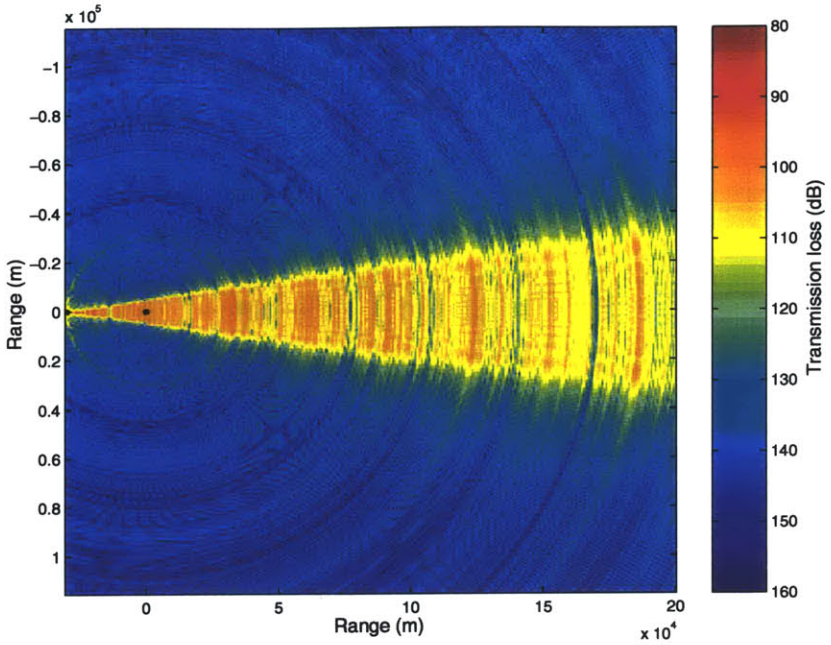

Parameters: I = 1. R_I = .5 m. Depth = 1000 m. Source at (-3000 m, 0, 1000 m).

Figure 4-7: No seamount. $\mu = 0 \ldots 1300$

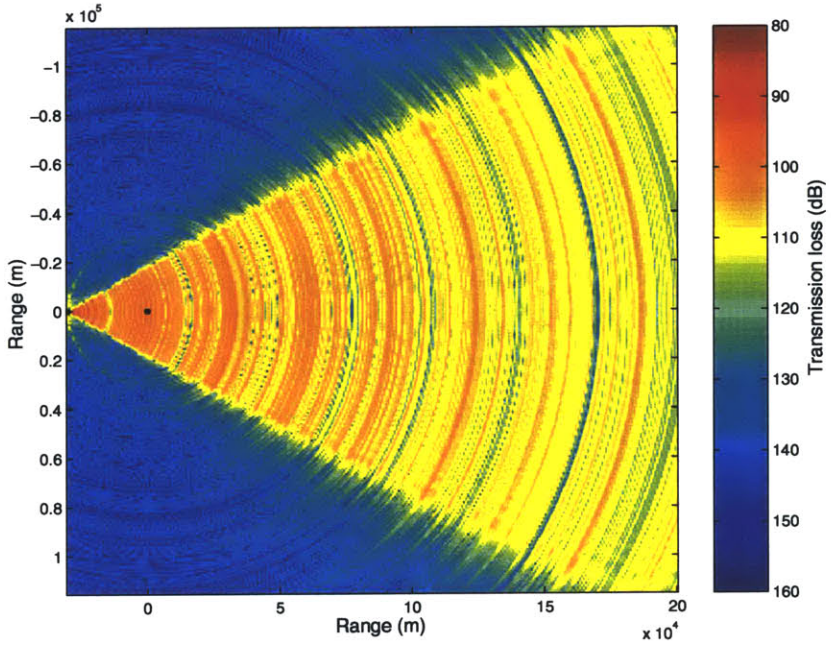

Parameters: I = 1. R_I = .5 m. Depth = 1000 m. Source at (-3000 m, 0, 1000 m).

4.3 Cylinders

The simplest case is the modeling of the seamount into one cylinder of radius equal to the base radius of the seamount. Of course, this case is not physically realistic, but it helps to determine the validity domain of the code.

4.3.1 Validity domain of the results

Figure 4-8 shows the results obtained for a cylinder of radius $R_I = 5000\,\text{m}$.

Figure 4-8: Cylinder of radius $R_I = 5000\,\text{m}$

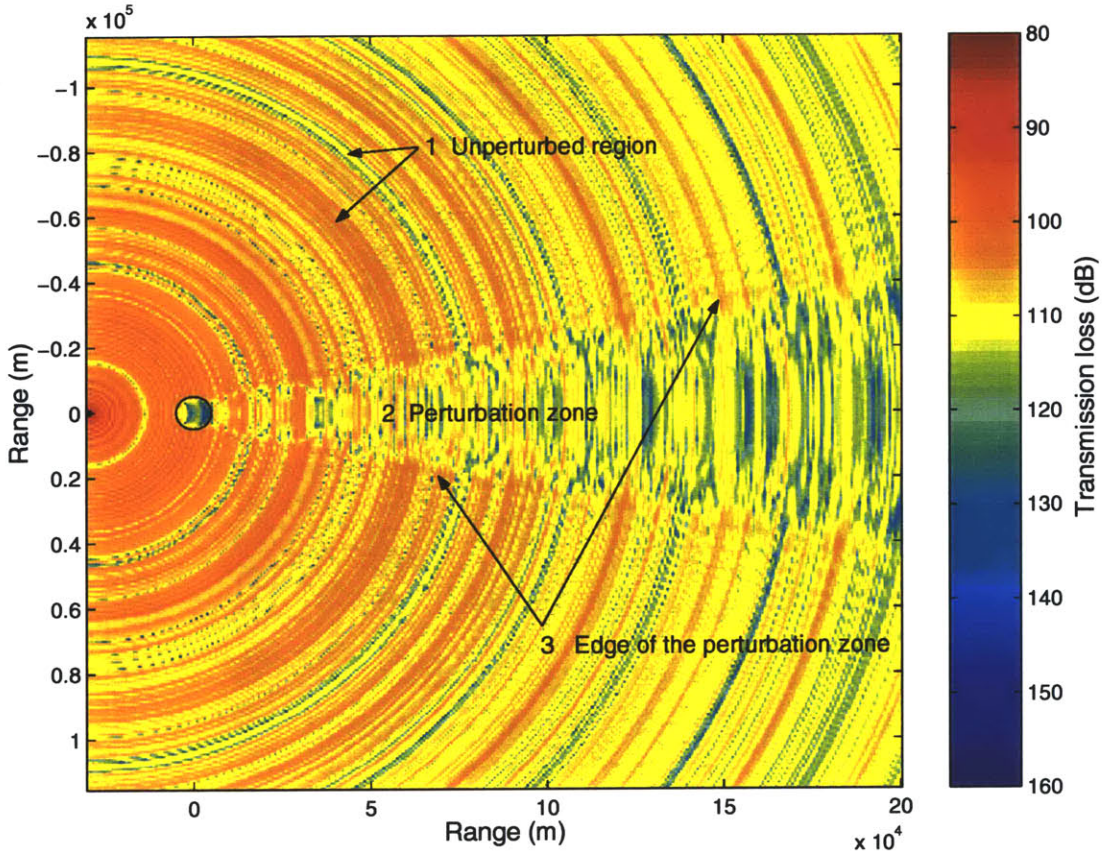

Parameters: I = 1. R_I = 5000 m. Depth = 1000 m. Source at (-3000 m, 0, 1000 m).

Three different regions can be observed in the figure.

- The coaxial circular patterns in the unperturbed region, indicated by arrows 1,

are attributed to the sound propagation in the waveguide between the sea surface and the sea bed, as illustrated in figure 4-4.

- The perturbation zone inside and behind the cylinder, labelled number 2, is attributed to the presence of the cylinder.
- The edge of the perturbation zone, indicated by arrows 3, is attributed to the reflection and diffraction at the cylinder surface.

The perturbation zone

The perturbation zone does not end abruptly but vanishes as the distance from the seamount increases. Far from the seamount, the sound pressure inside this zone just takes the values of the unperturbed region.

It is contained in a region bounded by two lines going from the source and tangent to the cylinder.

In this case, the perturbation zone 2 is a shadow zone: the sound pressure level is lower than in zone 1. We will see in later figures that this is not always the case. Sometimes the perturbation zone contains a higher sound pressure level than outside of it.

Computational discontinuity

To understand how the pressure is computed in the case of a decomposition into several rings, we must know how the pressure is computed as a function of circumferential orders in the simple case of a cylinder. In the example of figure 4-8, the coefficients of the solution vectors X_μ become null for $\mu > 561$, except for coefficients $(C_{\mu,\nu})_{\nu\in[1;N]}$ (this result is of course obtained by numerical computation). I designate the "critical μ" $(= 561)$ as μ_{cr}. In a more mathematical expression,

$$\forall \mu > \mu_{cr}, \forall \nu = 1 \ldots N, \forall i = 1 \ldots I, E^i_{\mu\nu} = F^i_{\mu\nu} = B_{\mu\nu} = 0,$$
$$\text{and } \forall \mu > \mu_{cr}, \forall \nu = 1 \ldots N, C_{\mu\nu} = \frac{-i\pi}{2}.$$

This indicates that, for $\mu > \mu_{cr}$, the numerical computation yields results as if there were no cylinder. The results for $\mu = 0 \ldots 561$ are in figure 4-9.

Figure 4-9: Cylinder of radius $R_I = 5000\,\text{m}$. $\mu = 0 \ldots 561$

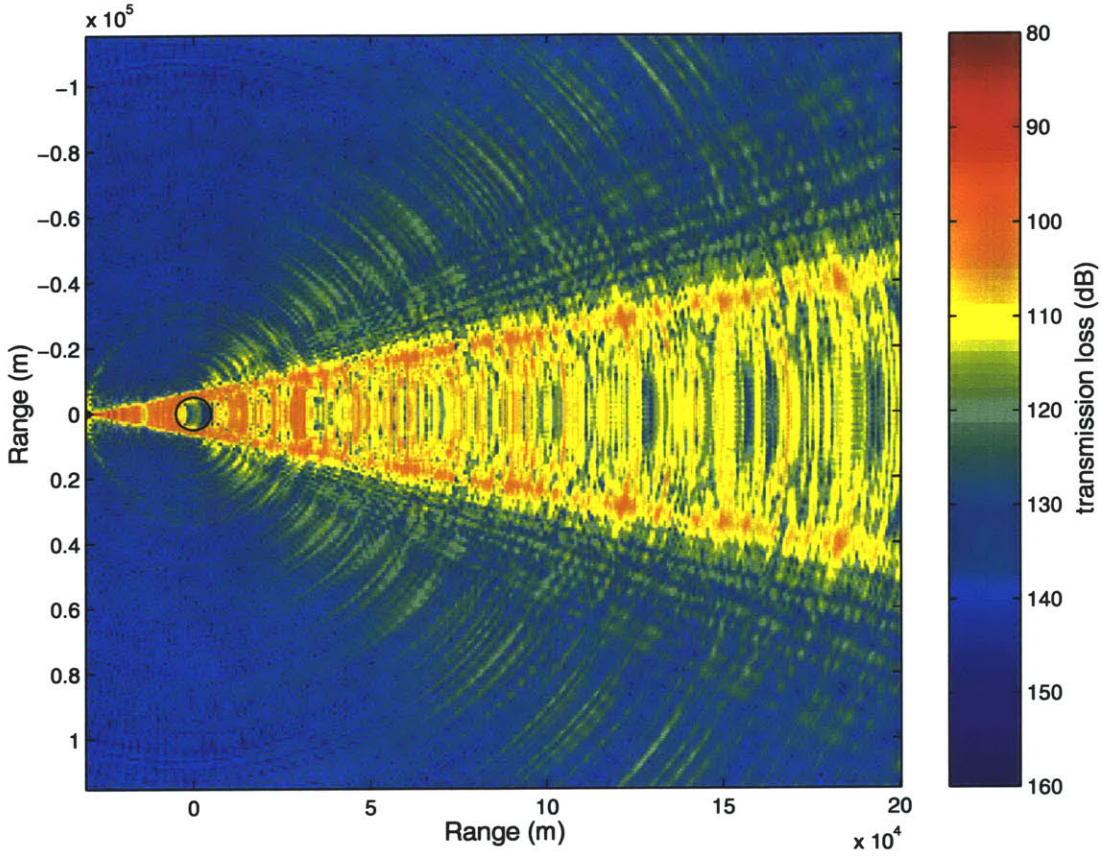

Parameters: I = 1. R_I = 5000 m. Depth = 1000 m. Source at (-3000 m, 0, 1000 m).

I showed in the previous section that the computation produces results that fill the environment starting from axis $\phi = 0$ and spreading toward axes $\phi = \frac{\pi}{2}$ and $\phi = \frac{-\pi}{2}$. Since the perturbation region is behind the seamount and along axis $\phi = 0$, it is filled by computations made for low circumferential orders. By comparing figures 4-8 and 4-9, we see that the perturbation zone behind the cylinder stops around $\mu = 561$. For $\mu > 561$, the results are similar to those in figure 4-4.

For $\mu < 561$ and μ close to 561 (i.e., at the edge of the perturbation zone), coefficients $E^i_{\mu\nu}$, $F^i_{\mu\nu}$ and $B_{\mu\nu}$ are close to 0 (in the order of 10^{-40}). Thus the discontinuity

is not easy to notice.

This discontinuity in the numerical results happens when systems 3.52 are solved. In order to solve them, I used subroutines from the LAPACK package, the best available tool for solving systems of simultaneous linear equations [22].

In conclusion, the results both inside and outside the perturbation zone are accurate, but the results along the frontier of the perturbation zone are subject to numerical discontinuity. On the scale of my problem, the discontinuity is not noticeable.

4.3.2 Example of perturbation zone with a high sound pressure level

In some cases, I obtain perturbation zones in which the sound pressure level is higher than outside of it, for the same distance from the source. For instance, it happens for a cylinder of radius $R_I = 10\,\text{km}$, as illustrated in figure 4-10. In this case the edge of the perturbation zone has a lower sound pressure.

Figure 4-10: Cylinder of radius $R_I = 10\,\text{km}$. Depth = 1000 m

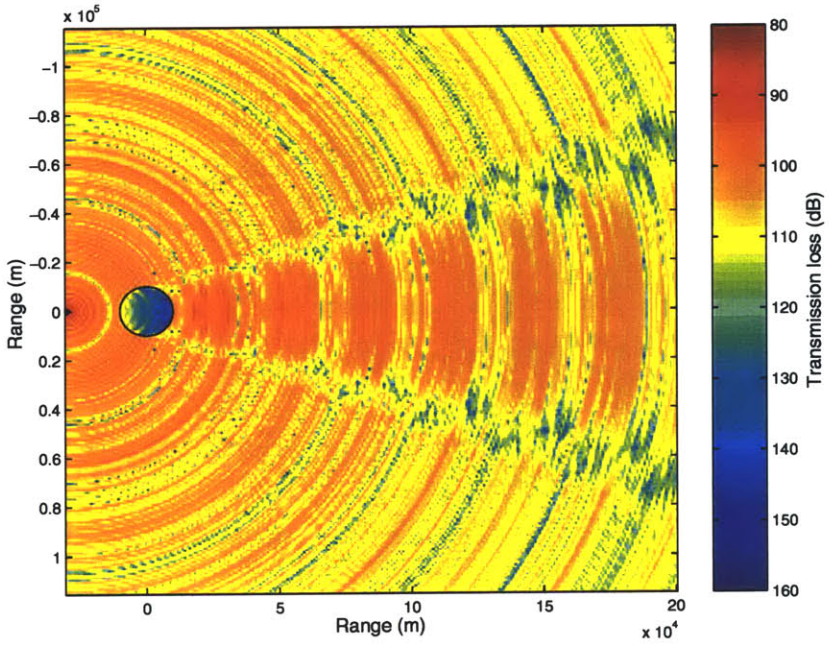

Parameters: I = 1. R_I = 10 km. Depth = 1000 m. Source at (-3000 m, 0, 1000 m).

Three-dimensional solution

Figure 4-11 shows the results at 500 m below the surface, and figure 4-12 shows the results at 3000 m below the surface.

The mapping of the sound propagation is obviously not the same in figures 4-10, 4-11 and 4-12. Thus, the model effectively takes the three-dimensional character of the problem into account. The general aspect of the perturbed zone remains the same: it is about the same width and there is still a higher sound pressure inside of it than outside for the same distance from the source.

Figure 4-11: Cylinder of radius $R_I = 10\,\text{km}$. Depth = 500 m

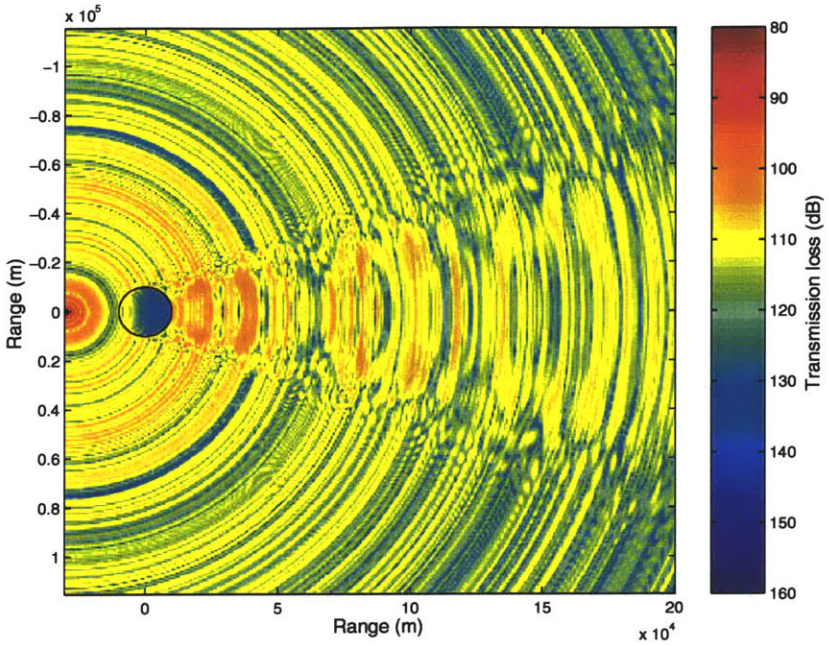

Parameters: I = 1. R_I = 10 km. Depth = 500 m. Source at (-3000 m, 0, 1000 m).

Figure 4-12: Cylinder of radius $R_I = 10\,\text{km}$. Depth = 3000 m

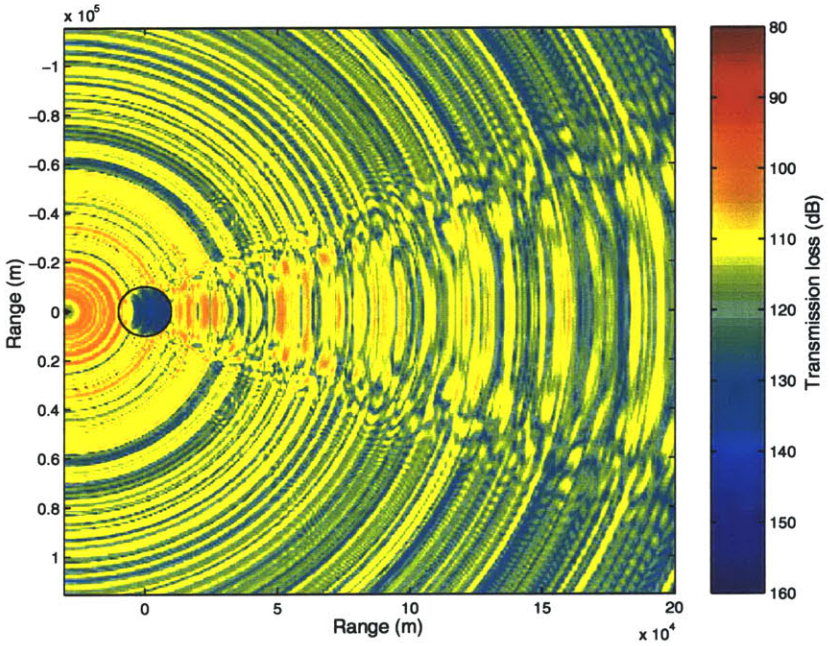

Parameters: I = 1. R_I = 10 km. Depth = 3000 m. Source at (-3000 m, 0, 1000 m).

4.4 Decomposition of the seamount into several rings - Final results

The dimension of the system is $N \times (2I + 1) \times (M + 1)$, so the more rings in the decomposition, the bigger the dimension and the longer it takes to solve the problem. For this reason, I did not decompose the seamount in more than 10 rings.

Figure 4-13 shows the results for a decomposition of the seamount into 2 rings.

Figure 4-13: Decomposition of the seamount into 2 rings

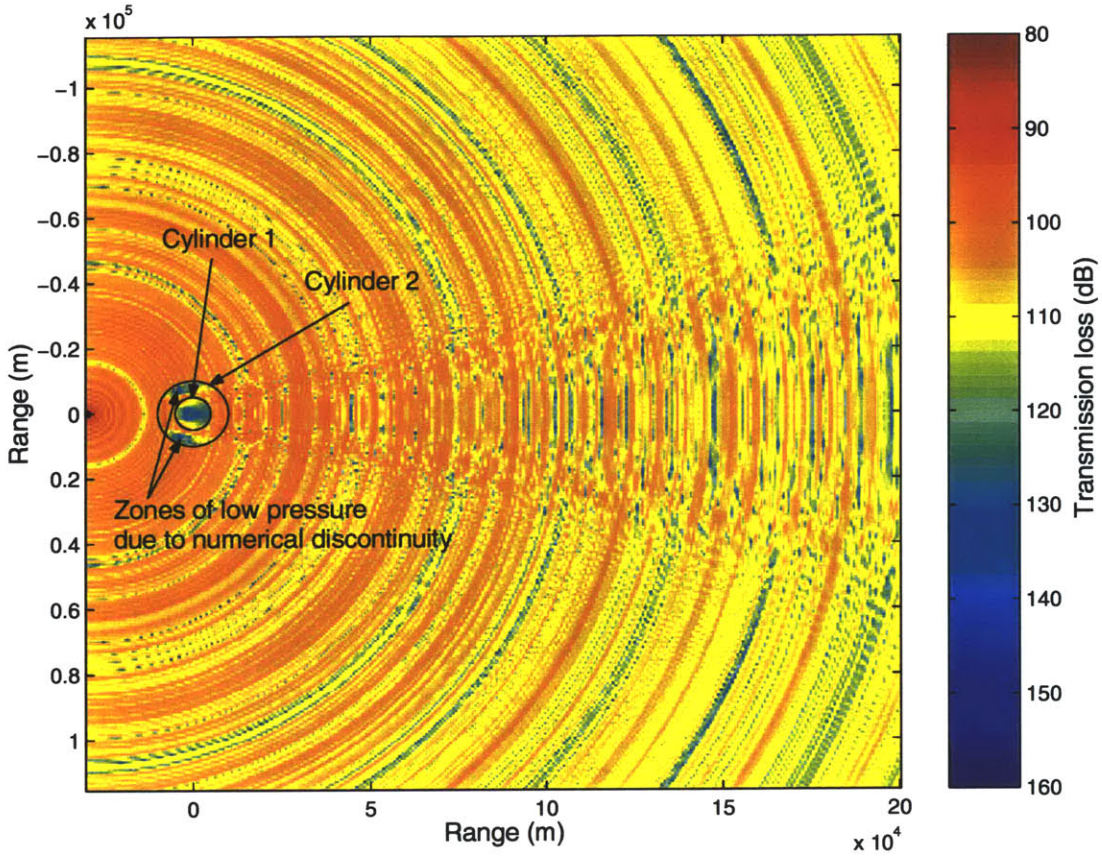

Parameters: I = 2. R_I = 10 km. Depth = 1000 m. Source at (-3000 m, 0, 1000 m).

The cylinder at the depth of the receiver (1000 m) has a diameter equal to 5000 m.

The system behaves like described in section 4.3: at a certain μ_{cr}, the solutions will become the same as if there were no seamount. This happens outside of the

perturbation zone generated by the cylinder of diameter 5000 m. The problem here is that coefficients $E^2_{\mu\nu}$ and $F^2_{\mu\nu}$ are used to compute the sound pressure field in the inner region ($r < R_I$), so when they become null, the sound pressure becomes null in the inner region. It creates some zones on the sides of the seamount that are filled with a sound pressure level that is lower than it should. This problem is just a numerical problem and has no physical meaning.

In this case, the results are valid in the same regions than the results for cylinders (section 4.3): Results are valid inside the perturbation region and outside of it. The discontinuity occurs near the edge of the perturbation region. However, it is small enough to be invisible for $r > R_I$ i.e., in the external region.

By comparing Figure 4-8 and Figure 4-13, we can notice that, even if the diameters of the cylinders at depth 1000 m are the same, the perturbation zones look very different. In the case of Figure 4-13, where the seamount is decomposed into two rings, the perturbation zone contains much higher values of the sound level than in Figure 4-8 where the seamount is reduced to a cylinder. Thus we can see that the model is sensitive to the number of rings taken in the decomposition.

Figure 4-14 is another example in which discontinuity in the solution of linear systems 3.52 produces wrong results for $r < R_I$. In this case, the seamount is decomposed into 10 rings. The cylinder that is at detph 1000 m has a diameter of 3000 m.

Figure 4-14: Decomposition of the seamount into 10 rings

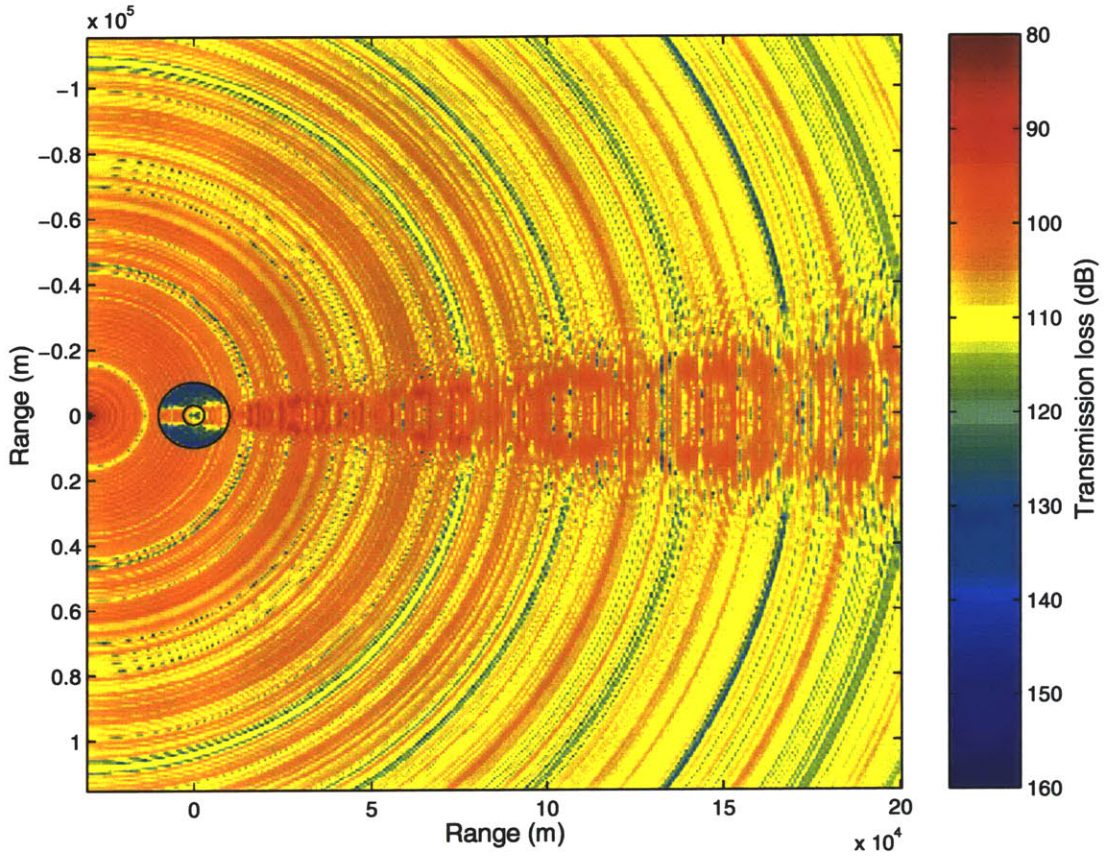

Parameters: I = 10. R_I = 10 km. Depth = 1000 m. Source at (-3000 m, 0, 1000 m).

There is the same problem as previously: outside the perturbation zone, coefficients $E^i_{\mu\nu}$ and $F^i_{\mu\nu}$ become null and there appear some regions in the sides of the seamount where the pressure is 0 for $\mu > \mu_{cr}$.

However, the discontinuity is too small to be visible in the external region.

4.5 Conclusion

The computation is limited by the precision of the computational tools available to solve linear systems $\mathcal{A}_\mu.X_\mu = \mathcal{B}_\mu$ (3.52). However, some conclusions can be deduced from the results we obtain.

Filling of the environment as a function of circumferential order

The computation produces results that fill the environment starting from axis $\phi = 0$ and cylindrically spreading toward axes $\phi = \frac{\pi}{2}$ and $\phi = \frac{-\pi}{2}$ as the circumferential order increases.

The shape of the perturbation zone

The perturbation zone behind the seamount is computed without being disturbed by the discontinuity in the calculus at μ_{cr}. It fills the region enclosed in two lines going from the source and tangent to the cylinder that is at the depth of the receiver. It does not end abruptly but vanishes with distance.

The values inside the perturbation zone

The sound pressure level inside the perturbation zone can be either higher or lower than the sound pressure outside. Although the difference between the sound pressure levels of the two zones varies, it always stays in the order of 10 dB.

Validity of the method

By comparing Figure 4-13 and 4-8, we can conclude that the model is sensitive to the number of rings in the decomposition. Moreover, the mathematical method employed always produces stable systems to solve.

The discontinuity that occurs after μ_{cr} is simply due to the fact that the subroutines used to solve the system are not precise enough to compute results below 10^{-40}. The discontinuity is only visible in some regions on the sides of the seamount but for all $r > R_I$, it is small enough to consider that the results are valid.

Chapter 5

Conclusion

5.1 Summary

In this thesis, I compiled two mathematical models to compute the sound propagation around conical seamounts:

- Taroukadis's modeling of the seamount as a superposition of rings [7],
- Schmidt and Jensen's Direct Global Matrix approach [4].

The mathematical models lead to an analytically well conditioned system of linear equations. This ensure stability when solving the system for long range.

Satisfying results can be obtained in the case of cylinders: we can see a perturbation zone behind the seamount and analyze its shape and values. It is bounded by two lines going from the source and tangent to the cylinder. It can contain values that are higher or lower than outside of it for the same distance from the source. (In the later case, it can be called a "shadow zone.")

A discontinuity occurs in the solution, because even the best subroutines available to solve the system lose precision for small numbers. This discontinuity is too small to be noticeable at the scale of our problem.

If we decompose the seamount into several rings, the same kind of discontinuity in the solutions prevents us from getting valid results inside the region of the seamount.

However, as in the cases of cylinders, the discontinuity is small enough to be invisible outside of the region of the seamount.

The results obtained show that the model is sensitive to the decomposition into rings. The perturbation zone behind the seamount has the same characteristics than in the case of cylinders.

5.2 Future work

Opportunities to extend the work described in this thesis abound. Two areas can be emphasized: simulation and real-world acoustics. This document dealt entirely with a fictitious simulated ocean. Areas which can be improved are:

- *Use of different subroutines to solve the system.* Although I used the best available subroutines for solving this kind of systems [22], a subroutine especially designed for the problem may be able to avoid the numerical discontinuity at μ_{cr}.

- *Experimental verification.* One could conduct deep water experiments to verify the data that I obtain by numerical simulation, especially the results about the shape of the perturbation zone. Most of the experiments that have been done for such environments just provide measurements of the sound pressure along axis $\phi = 0$. It could be interesting to verify the triangular shape of the perturbation region by taking measurements along lines perpendicular to axis $\phi = 0$.

Appendix A

Nomenclature

p	=	acoustic pressure
c	=	sound speed $= c_0 + i\,c_1$
T	=	temperature
S	=	salinity
h	=	depth of the sea bottom
h_E	=	depth of the sediment layer
R_I	=	radius of the base of the seamount
ρ_1	=	density of water
ρ_2	=	density of the sediment layer
$\overrightarrow{n}$	=	unit normal vector outside the sediment layer
S_{bm}	=	surface of the seamount
S_b	=	surface of the sediment layer
$(R_0, 0, z_0)$	=	coordinates of the source. $z_0 = 1000\,\mathrm{m}$
f	=	frequency $= 20\,\mathrm{Hz}$
k	=	wavenumber $= \omega/c(z) = k_0 + ik_1$
k_n	=	radial wavenumber for the mode $n = k_{n0} + ik_{n1}$
$R_{mn}(r)$	=	radial eigenfunction for the circumferential mode m and the vertical mode n
$U_n(z)$	=	depth eigenfunction for the vertical mode n
$\psi_m(\phi)$	=	circumferential eigenfunction for the circumferential order m

R_i	=	radius of the ith ring
h_i	=	depth of the ith ring
α	=	absorption coefficient
$H_\mu^{(1)} = H_\mu$	=	Hankel function of the first kind of order μ
J_μ	=	Bessel function of order μ
N	=	number of vertical orders in the normal decomposition
M	=	number of circumferential orders in the normal decomposition

Subscripts

m, μ	=	circumferential order
n, ν	=	vertical order
i	=	ith ring

Superscripts

$E = I + 1$	=	external field
I	=	inner field
i	=	ith ring

Appendix B

Computing technical details

This thesis was done entirely using IBM-PC compatible computers running the Linux operating system. Linux is a free OS for computers using the Intel and Alpha microprocessors. More information on Linux can be obtained from http://www.linux.org/.

The acoustic propagation code that was employed is the KRAKEN Normal Mode Program [21], by Mike Porter of Naval Research Laboratory. The sources were obtained from http://oalib.saic.com/pub/oalib/AcousticsToolbox/at.tar.Z, and compiled on PCs using gcc and f77.

The subroutines used to solve systems 3.52 come from the LAPACK package [22]. The main subroutine used was ZGBSV, the driver routine for solving double precision complex band matrices. The sources were obtained at http://netlib2.cs.utk.edu/lapack/. They were compiled using f77 on PCs and fort on Alpha workstations.

The subroutines used to compute Hankel and Bessel functions come from the package ZBSUBS [23], by Donald Amos of Sandia National Laboratories. To compute Hankel functions, I used the subroutine ZBESH and to compute Bessel functions, I used the subroutine ZBESJ. They were compiled using f77 on PCs and fort on Alpha workstations.

My code was entirely written in ANSI C and compiled with gcc on PCs and ccc on Alpha workstations.

I used MATLAB to display the results. MATLAB is a technical computing

environment for numerical computation and visualization, marketed by The Math Works (http://www.mathworks.com/).

The code was running in parrallel on 7 computers among which were six PCs (one 333 MHz Pentium II, two 400 MHz Pentium II, two 600 MHz Pentium III, and one 600 MHz K7 microprocessors), and one Alpha workstation (with a 667 MHz EV67 microprocessor). The code was taking a great amount of time to run: between one week and ten days were necessary to obtain the results presented in chapter 4.

Bibliography

[1] David A. Nutile and Albert N. Guthrie, "Acoustic shadowing by seamounts," J. Acoust. Soc. Am., vol. 66, pp. 1813-1817, 1979.

[2] Gordon R. Ebbeson and R. Glenn Turner, "Sound propagation over Dickins Seamount in the Northeast Pacific Ocean," J. Acoust. Soc. Am., vol. 73, pp. 143-152, 1983.

[3] N. Ross Chapman and Gordon R. Ebbeson, "Acoustic shadowing by an isolated seamount," J. Acoust. Soc. Am., vol. 73, pp. 1979-1984, 1983.

[4] F. B. Jensen, W. A. Kuperman, M. B. Porter, and H. Schmidt, *Computational Ocean Acoustics* (American Institute of Physics, New York, 1994).

[5] C. H. Harrison, "Acoustic shadow zones in the horizontal plane," J. Acoust. Soc. Am., vol. 65, pp. 56-61, 1979.

[6] G. A. Athanassoulis and A. M. Prospathopoulos, "Three-dimensional acoustic scattering of a source-generated field from a cylindrical island," J. Acoust. Soc. Am., vol. 100, pp. 206-218, 1996.

[7] M. I. Taroukadis, "A coupled-mode formulation for the solution of the helmoltz equation in water in the presence of a conical seamount," Journal of Computational Acoustics, vol.4, pp. 101-121, 1996.

[8] H. Schmidt and F. B. Jensen, "A full wave solution for propagation in multilayered viscoelastic media with application to Gaussian beam reflection at fluid-solid interfaces," J. Acoust. Soc. Am., vol. 77, pp. 813-825, 1985.

[9] H. Schmidt, "Numerically stable global matrix approach to radiation and scattering from spherically stratified shells," J. Acoust. Soc. Am., vol. 94, pp. 2420-2430, 1993.

[10] D. C. Ricks and H. Schmidt, "A numerically stable global matrix method for cylindrically layered shells excited by ring forces," J. Acoust. Soc. Am., vol. 95, pp. 3339-3349, 1994.

[11] G. V. Frisk, *Ocean and Seabed acoustics* (Prenctice Hall, New Jersey, 1994).

[12] M. B. Porter, *The KRAKEN Normal Mode Program Manual* (Naval Research Laboratory, Whashington, DC, 1992).

[13] H. Medwin and C. S. Clay, *Fundamentals of Acoustical Oceanography* (Academic Press, San Diego, 1997).

[14] J. Sellschopp, "Towed thermistor chain data collected during the cruise NORDMEER 87," Rep. FWG-87-4 (Forschungsanstalt der Bundeswehr für Wassershall- und Geophysik, Kiel, Germany, 1987).

[15] R. J. Urick, *Sound propagation in the sea* (Defense Advanced Research Projects Agency, Whashington, DC, 1979).

[16] E. G. Williams, *Fourier acoustics - Sound Radiation and Nearfield Acoustical Holography* (Naval Research Laboratory, Whashington, DC, 1999).

[17] F. W. Olver, Bessel functions of integer order. In M. Abramovitz and I. A. Stegun, editors, *Handbook of Mathematical Functions*, chapter 9, pp. 355-433, Dover, 1972.

[18] D. C. Ricks, "Elastodynamic modeling of fluid-loaded cylindrical shells with multiple layers and internal attachments," thesis, Massachusetts Institute of Technology, Cambridge, MA, May 1994.

[19] R. J. Urick, *Principles of Underwater Sound* (McGraw-Hill, New York, 1983).

[20] E. Zauderer, *Partial Differential Equations of Applied Mathematics* (John Wiley and Sons, New York, 1989).

[21] M. B. Porter, *The Kraken Mode Program* (Naval Research Laboratory, Whashington, DC, 1992).

[22] E. Anderson, Z. Bai, C. Bischof, L. S. Blackford, J. Demmel, J. Dongarra, J. Du Croz, A. Greenbaum, S. Hammarling, A. McKenney, and D. Sorensen, *LAPACK User's Guide* (Society for Industrial and Applied Mathematics, Philadelphia, PA, 1999).

[23] D. E. Amos, *ZBSUBS.FOR: Double precision subroutines* (Sandia National Laboratories, Albuquerque, NM, 1993).